Atmos. Chem. Phys. Discuss., 13, 24343–24403, 2013
www.atmos-chem-phys-discuss.net/13/24343/2013/
doi:10.5194/acpd-13-24343-2013

Atmospheric Chemistry and Physics Discussions

CARIBIC DOAS observations of nitrous acid and formaldehyde in a large convective cloud

K.-P. Heue[1,2], H. Riede[1], D. Walter[1,2], C. A. M. Brenninkmeijer[1], T. Wagner[1], U. Frieß[2], U. Platt[2], A. Zahn[3], G. Stratmann[4], and H. Ziereis[4]

[1]Max-Planck-Institut für Chemie (MPIC), Mainz, Germany
[2]Institut für Umweltphysik (IUP), Universität Heidelberg, Heidelberg, Germany
[3]Institut für Meteorologie und Klimaforschung (IMK), Karlsruhe, Germany
[4]Deutsches Zentrum für Luft- und Raumfahrt (DLR), Institut für Physik der Atmosphäre, Weßling, Germany

Received: 12 August 2013 – Accepted: 4 September 2013 – Published: 16 September 2013

Correspondence to: K.-P. Heue (klaus-peter.heue@mpic.de)

Published by Copernicus Publications on behalf of the European Geosciences Union.

Abstract

The CARIBIC (Civil Aircraft for the Regular Investigation of the atmosphere Based on an Instrument Container) flying laboratory measures once per month the chemical composition at cruise altitude (10...12 km) during 4 consecutive Lufthansa flights. Here we present a case study of enhanced nitrogen oxides (NO_x), nitrous acid(HONO), and formaldehyde (HCHO) in a thunderstorm cloud over the Caribbean islands of Guadeloupe in August 2011. Nitrous acid is an important reservoir gas for OH radicals, and only few observations of HONO at cruise altitude exist. CARIBIC is designed as a long period atmospheric observation system, the actual system has been flying almost monthly since 8 yr now. During this period only very few similar events (one since 2008) were observed.

Due to multiple scattering the light path inside clouds is enhanced, thereby lowering the detection limit of the DOAS instrument. Under background conditions the detection limits are 46 ppt for HONO, 387 ppt for HCHO, and 100 ppt for NO_2 and are roughly three times lower inside the cloud. Based on radiative transfer simulations we estimate the path length to 90...100 km and the cloud top height to ≈15 km. The inferred mixing ratios of HONO, HCHO and NO_2 are 37 ppt, 400 ppt and 170 ppt, respectively. Bromine monoxide (BrO) remained below the detection limit of 1 ppt.

Because the uplifted air masses originated from the remote marine boundary layer and lightning was observed in the area by the World Wide Lightning Location Network several hours prior to the measurement, the NO (≈1.5 ppb) enhancement was in all likelihood caused by lightning. The main source for the observed HCHO is probably updraught from the boundary layer, because the chemical formation of formaldehyde due to methane oxidation is too weak. Besides HCHO also CH_3OOH and isoprene are considered as precursors.

The chemical box model CAABA is used to estimate the NO and HCHO source strengths, which are necessary to explain our measurements. For NO a source strength of 8.25×10^9 molec cm^{-2} s^{-1} km^{-1} is found, which corresponds to the light-

ACPD
13, 24343–24403, 2013

ning activity as observed by the World Wide Lightning Location network and a lightning emission of 4.2×10^{25} NO molec/flash. The HCHO updraught is of the order of 121×10^9 molec cm^{-2} s^{-1} km^{-1}. Also isoprene and CH_3OOH as possible HCHO sources were studied and similar source strengths were found.

1 Introduction

Nitrous acid (HONO) and especially its relevance for OH production and hence photochemistry has been studied for many years (Platt et al., 1980). Despite this, the experimental dataset of HONO is very limited due to the low abundance and general difficulty to measure this elusive species. Most studies dealt with the production of HONO on surfaces in the boundary layer and airborne measurements are scarce. Here we report on the measurement of HONO by DOAS on a passenger aircraft while flying through a large cloud system during which also formaldehyde was detected. Because very few such cases are known at all, and HONO specific papers are rare, we will first introduce the reactions involved in its production. Also some of the main sources of upper tropospheric formaldehyde are briefly summarised.

Nitrous acid accumulates during the night and initializes the photo-oxidation processes when photolysed just after sunrise. Its three main sources are direct emissions, chemical formation on surfaces, and production in the gas phase. Its main sinks are photolysis and the reaction with OH.

$$2NO_2 + H_2O \xrightarrow{\text{surface}} HONO + HNO_3 \quad \text{(R1)}$$

$$NO + OH \xrightarrow{M} HONO \quad \text{(R2)}$$

$$HONO \xrightarrow{h\nu} OH + NO \quad (\lambda < 400\,\text{nm}) \quad \text{(R3)}$$

$$HONO + OH \rightarrow NO_2 + H_2O \quad \text{(R4)}$$

The Reactions (R2) and (R3) involve HONO as an intermediate storage of OH. They lead to a photo-stationary state with neither destruction nor formation of OH, which is

ACPD
13, 24343–24403, 2013

slightly changed, when R4 is included. The OH radical is however definitely removed by the reaction with NO_2:

$$OH + NO_2 \xrightarrow{M} HNO_3 \quad \text{(R5)}$$

The main sink of HNO_3 is wash out, because the photolysis is too slow to reproduce OH.

The overall fate of OH therefore depends on the ratio of NO (recycling) to NO_2 (wash out). The ratio NO over NO_2 depends on the titration of NO by O_3 and the photolysis frequency of NO_2 :

$$NO + O_3 \rightarrow NO_2 + O_2 \quad \text{(R6)}$$

$$NO_2 \xrightarrow{h\nu} NO + O \quad \text{(R7)}$$

$$O + O_2 \xrightarrow{M} O_3 \quad \text{(R8)}$$

These reactions lead to the photo-stationary Leighton ratio.

$$L = \frac{NO}{NO_2} = \frac{J_{R7}}{O_3 \cdot k_{R6}} \quad (1)$$

The reaction constant k_{R6} as well as any other reaction constant used in the following were taken from Atkinson et al. (2004) or (2006) respectively, the temperature dependence was considered and unless stated differently, a temperature of −50 °C was used. In the boundary layer the Leighton ratio is typically less than 1, however, in the upper troposphere ($T = -50\,^{\circ}C$, $p = 205\,hPa$, $O_3 = 40\,ppb$) reach up to 10, especially for the conditions we focus on in this paper. Furthermore in cloud tops the solar radiation is enhanced by a factor up to 3 (2...5 Brasseur et al., 2002) and therefore the photolysis frequency J_{R7} increases and the Leighton ratio reaches up to 30. Under these conditions OH radicals have a low probability of getting lost, which leads to a large HONO formation rate on top of high reaching thunderstorm clouds. In thunderstorm clouds NO

ACPD
13, 24343–24403, 2013

peak values up to 7 ppb were found (Huntrieser et al., 2009). Simulations by Bhetanabhotla et al. (1985) predicted a lightning HONO to NO emission ratio of 6.7×10^{-3}. The product of the simulated HONO to NO ratio and the measured NO peak values results in initial peak values of 47 ppt HONO caused by lightning. However, Dix et al. (2009) found higher values (70 ppt) averaged over a long light path in a polluted updraught.

Despite the expected high formation rate in cloud tops airborne HONO measurements are scarce. Zhang et al. (2009) performed measurements in the boundary layer and above up to 2600 m. They mainly confirmed the previous profile studies at towers, namely that there is a strong decrease in the HONO mixing ratio with height. Up to 74 ppt were measured in the boundary layer and a range of 4 to 17 ppt above. They concluded that the main sources for HONO are close to the ground. Jurkat et al. (2011) measured HONO at cruise altitude in aeroplane plumes to estimate air traffic HONO formation, and found up to 1.2 ppb HONO and 65 ppb NO. Dix et al. (2009) also using the DOAS instrument on the CARIBIC platform found 70 ppt of HONO, 280 ppt NO_2, and 550 ppt HCHO over central China (106.5° E, 27.1° N) in August 2006. In the vicinity of the cloud also NO, NO_y, CO and O_3 were enhanced, which indicates that a strong updraught of polluted boundary layer air had occurred. More details of this event are given in Dix (2007).

More information is available for formaldehyde in the upper troposphere. Under background conditions between 40 ppt (over the Pacific, Fried et al., 2003) and 200 ppt (over Europe, Stickler et al., 2006) are observed. The main HCHO source in the remote atmosphere is methane oxidation, the destruction is mainly given by photolysis and reaction with OH. Next to methane, methyl hydroperoxide (CH_3OOH), isoprene and acetone are additional important precursors. Isoprene reacts with OH and yields 50 % formaldehyde and about 40 % for the reaction with O_3 (Carter and Atkinson, 1996). The photolosis of acetone results in CH_3CO and CH_3, which with subsequent reactions yields formaldehyde. Several sensitivity studies showed a strong positive correlation between HCHO concentration and NO_x (Stickler et al., 2006, and references therein).

ACPD
13, 24343–24403, 2013

In this study we present CARIBIC-DOAS observations of HONO, NO_2 and HCHO inside a large cloud system over the Caribbean islands of Guadeloupe. To our knowledge, this is the second only publication about nitrous acid in a deep convective cloud, after Dix et al. (2009). Whereas Dix et al. (2009) (also using CARIBIC) detected HONO in a cloud system over China under polluted conditions, here we deal with uplifted clean oceanic air. The islands of Guadeloupe (France) have about 0.4 million inhabitants and no significant industry (wikipedia.org, May 2013), therefore the local pollution levels can be expected to be low in relation to the dimension of the cloud of 480 km.

Nitrous acid was also detected on other occasions with the CARIBIC DOAS instrument, namely when the aeroplane flew over clouds. In most cases the HONO slant column densities (SCD) are close to the detection limit ($1 \ldots 2 \times 10^{15}$ molec cm^{-2}). Due to the shielding effect of the cloud the O_4 SCDs are low in all these cases. On the other hand there are cases where comparable low O_4 SCDs are observed but no increase in HONO is found. In the last 20 flight sequences (July 2011...June 2013) about 100 cases were observed where the O_4 SCD was significantly reduced, and HONO was detected in 50 cases. A more general study focussing on the all these HONO observations and the reduced O_4 column densities might be published later. Due to the high column densities inside the cloud, and the enhancement in HCHO and NO_x we will focus on this special event here.

2 The CARIBIC Instruments and the CAABA box model

The CARIBIC instrument container is installed on a Lufthansa Airbus A340-600 retrofitted with a 3 probe (trace gases, water and aerosol) inlet system. The aeroplane carries the instrument container on a monthly basis during four consecutive regular passenger flights for 2...3 days. CO, CO_2, O_3, NO, NO_2, NO_y (Sect. 2.2), CH_4, some organic compounds (e.g. acetone), mercury, total and gaseous water (Sect. 2.1) are measured in real time. Aerosols are measured for diameters larger than 4 nm, 12 nm and 18 nm with 3 CPCs and from 117 nm to 1.3 µm with an OPC. In addition, 16 aerosol

ACPD
13, 24343–24403, 2013

samples and 116 air samples are collected for post flight laboratory analysis of aerosol elemental composition, (Nguyen et al., 2006) and of a host of trace gases (Schuck et al., 2009; Baker et al., 2010). A DOAS instrument (Sect. 2.3) adds a remote sensing capacity to complete the instrumental package using 3 miniature DOAS telescopes mounted in the pylon. A video camera in the inlet pylon takes a frame every second for post flight cloud cover analysis. The instruments are maintained and operated by nine scientific groups from institutes in Europe (http://www.caribic-atmospheric.com, May 2013).

The trace gas and aerosol measurements are complemented by standard in-flight observations (e.g. position, temperature, wind speed, pressure) provided by the aeroplane's ARINC system. The Royal Dutch Meteorological Institute (KNMI) supports the CARIBIC project with trajectory calculations along the flight track based on the TRAJKS model (Scheele et al., 1996; Stohl et al., 2001). Both forward and backward trajectories for 2 and 8 days respectively are calculated using ECMWF weather data interpolated to the position and time of the CARIBIC observation.

2.1 Water measurements

The CARIBIC container has two systems for water measurements (Brenninkmeijer et al., 2007). A chilled mirror frost point hygrometer (BUCK CR2) with a temporal resolution up to 3 min depending on the humidity, and a 2-channel photo-acoustic laser spectrometer with a temporal resolution of 3 s. The detection limit is 0.5 ppm and the accuracy is 0.4 K for the frost point hydrometer. The sensitivity of the photo-acoustic sensor may vary by a few percent within an hour, therefore the instrument is post flight calibrated by comparison with the frost point instrument. The inlet probe for water allows the measurement of total water (including cloud droplets) by using a forward pointing inlet and gaseous water by a second sidewards orifice. The forward facing inlet uses the ram pressure (60. . . 100 hPa) to transport the inlet air through inlet tubing to both instruments, frost point and photo-acoustic. The sidewards facing inlet is connected to the photo-acoustic sensor, only, and uses a diaphragm pump, installed

ACPD
13, 24343–24403, 2013

downstream. This set-up allows the measurement of total water and gaseous water in which the difference between the two quantities gives the cloud water content.

2.2 Nitrogen oxides measurements

The NO-NO_y instrument on CARIBIC uses a two channel chemiluminescence detector (Ecophysics CLD-790 SR) to measure NO with a time resolution of 1 s. Details on the instrument are given in Brenninkmeijer et al. (2007) and Ziereis et al. (2000). Catalytic conversion technique is used for NO_y measurements. Using H_2 as a reducing gas, NO_y species are reduced to NO inside a heated gold tube. Nitrogen monoxide is subsequently measured using chemiluminescence. During the flight discussed here the NO_y channel was switched off due to technical problems.

In-flight the background signal is measured every 10 min for about 1 min. The NO detectors are calibrated prior and after each flight sequence i.e. twice per month. The uncertainty of the NO measurements is about 8 % at 50 ppt NO.

2.3 DOAS on CARIBIC

The CARIBIC DOAS instrument has been described in detail in Dix et al. (2009) and Walter et al. (2012). The following basic description is taken from Heue et al. (2010). The DOAS instrument measures scattered sunlight and uses Differential Optical Absorption Spectroscopy (DOAS) (Platt and Stutz, 2008) to retrieve trace gas amounts in the atmosphere. The retrieved slant column density (SCD) is the absorber concentration integrated along the light path.

The SCD highly depends on the light path in the atmosphere. When measuring in or through clouds the light paths might be enhanced due to the scattering events on the cloud droplets. To estimate the length and the distribution of the light path, usually the measured O_4 SCDs are compared to model simulations. We used the three-dimensional Monte Carlo radiative transfer model "McAr-

ACPD
13, 24343–24403, 2013

tim" (Deutschmann et al., 2011) to estimate the cloud's extinction profile. Details on the properties of the simulated cloud are described in Sect. 3.1 and in the Appendix A.

The CARIBIC DOAS instrument observes scattered sunlight under three different elevation angles (−82°, −10°, +10° relative to the horizon). Three small telescopes present in the CARIBIC-pylon are connected to three spectrometers mounted in the container via quartz fibre bundles. The wavelength ranges of all spectrometers cover the interval from 300 to 400 nm with a spectral resolution of 0.5 nm (full width at half maximum). The time resolution is 8 s, which corresponds to 2 km horizontal resolution.

A fitting window from 328 to 378 mm (4 HONO absorption bands) was used to retrieve the slant column densities. A list of the included absorption cross sections including the Ring effect is given in Table 1. In a second fitting window (322...378 nm) another HCHO absorption band is included. The data are used for comparison. The spectral structures of the absorbers are clearly identified in both fitting windows, and the retrieved column densities agree well within the errors (Fig. 1).

For some co-added spectra (10 spectra co-added) we also tested the sensitivity of the SCD on the wavelength range between 320.9 and 353.3 nm for the lower end of the fitting window and from 360.9 to 395.0 for the upper end. Details on this method of the "retrieval wavelength fitting" can be found in Vogel et al. (2013). The fitting window had a minimum range of 300 channels and a maximum of 900 channels. The HONO SCD for the nadir spectrum (18:26:16...18:27:40 UTC) varied between 4.7×10^{15} molec cm^{-2} for the wavelength range 339.2...367.7 nm (2 HONO absorption bands) and 1.7×10^{15} molec cm^{-2} for 345.6 to 369 nm (1 HONO absorption band). In total 8379 wavelength intervals were considered, resulting in a mean SCD of $3.16 \pm 0.57 \times 10^{15}$ molec cm^{-2}. For the same spectrum the mean BrO SCD was $6.8 \pm 6.2 \times 10^{13}$ molec cm^{-2}, which demonstrates, that the BrO absorption cross section cannot be identified in this spectrum, because the SCD was below the detection limit.

In Table 2 the typical fit errors inside the cloud are given for the 8 s spectra. For HONO this error agrees well with the variation observed in the retrieval wavelength

ACPD
13, 24343–24403, 2013

fit, for BrO it is underestimated. In case ten spectra are added the error is reduced by a factor of ≈3. For unknown reasons the intensity in the −10° spectrograph was lower. As a consequence of that, the fit error is higher here compared to the other two spectrometers.

2.4 CAABA box model

CAABA (Chemistry As A Boxmodel Application) provides a flexible atmospheric chemistry box modelling framework (Sander et al., 2011). It features a modular structure, in which processes (e.g., emission and sedimentation), and simulation modes (e.g., Lagrangian simulations along trajectories) can be easily switched on and off independently. For the present study, the steady-state simulation mode was chosen, in which defined longer-lived chemical species are kept at fixed mixing ratios, while shorter-lived species adapt and equilibrate to the given boundary conditions, including temperature, humidity, pressure, solar zenith angle, and resulting reaction rates.

The atmospheric-chemistry reaction mechanism provided by the chemistry module MECCA is easily adaptable by preprocessing before the actual simulation: certain species, reaction types, or entire atmospheric domains can be selected or excluded. For the standard setup in this study, tropospheric gas-phase reactions were selected, comprising 448 species up to four C atoms, detailed isoprene chemistry, and 318 reactions of which 72 are photolytic. Halogen, sulphur, and mercury chemistry were excluded. As far as observations were available, they were included as input parameters of the model as detailed in Sect. 5.4.

3 Observations

During the flight to Caracas on 16 August 2011 the CARIBIC aeroplane flew through an extensive cloud system at 61.64° W and 16.19° N, over the Caribbean islands of Guadeloupe. While NO_x was enhanced, no enhancements in the typical pollution tracers CO,

ACPD
13, 24343–24403, 2013

CO_2, ethane or propane were measured (only CO is shown in Fig. 2). Also 15 min before or after the intersection of the cloud, none of these tracers were enhanced, including NO, which was measured at typical background levels of 100. . . 300 ppt. Ozone mostly showed an enhanced variability (± 5 ppb), which might be caused by an instrumental issue, and a slight decrease compared to the background level of 30. . . 40 ppb. The last whole air sample of this flight (No. 14) was collected while leaving the cloud (18:31:02 UTC). In the laboratory analysis, no enhancements in ethane, propane, butane or methyl chloride were found. Instead, compared to the preceding samples most mixing ratios were reduced (Table 3). However the two previous samples are not representative for the background conditions, as the trajectories originate from above the US coast. Because inside the cloud scavenging efficiently removes large particles (Ekman et al., 2006), the strong increase in the large aerosols (diameter between 117 and 1312 nm) is unexpected. It is however known that the break up of ice crystals, as can happen on the rim of the aerosol inlet shroud, leads to an increase in particles (Baumgardner et al., 2011).

The DOAS data showed a strong increase in O_4, which indicates a long light path inside the cloud. Moreover, the slant column densities for NO_2, HCHO and HONO were enhanced. The O_4 time series in -10° and in nadir show a strong decrease between 18:17 and 18:49 UTC (Fig. 3). On top of this reduction there is an even stronger increase at 18:25 UTC. A similar time series is found for $+10^\circ$, however the decrease is much smaller. The reduction in the O_4 column densities for both downward looking telescopes can be explained by a shielding effect of the cloud just below the aeroplane. Most of the detected light is reflected at the bright cloud by which the lower part of the atmosphere containing high O_4 concentrations is shielded. The strong increase is observed when the aeroplane is inside the cloud and is mainly caused by multiple scattering. Although the largest fraction of the observed light was probably scattered close to the flight altitude, the lower altitude levels also contribute to the O_4 signal (see Appendix A). The pictures taken by the video camera confirm this first interpretation of

ACPD
13, 24343–24403, 2013

the O_4 SCDs. A sketch of the cloud including the CARIBIC flight track above the cloud and through a part of it, is shown in Fig. 4.

It is interesting to note, that the HONO SCD in nadir and -10° increases and the O_4 SCD decreases, while flying above the cloud. Later on, when the aeroplane is inside the cloud, both O_4 and HONO reach their maximum SCDs. Therefore we conclude that there is no spectroscopic interference between HONO and O_4 which might have caused an artificial anti-correlation of these two slant column densities. The differences in the SCDs for each species and each viewing direction are also listed in Fig. 3. They are calculated as difference between the background and the maximum enhancement inside the cloud. Later on (Sect. 4) the retrieval of the mixing ratios is based on these values.

The horizontal expansion of the cloud can be estimated by multiplying the cruise velocity of the aeroplane (480 knots $\approx 248\,m\,s^{-1}$) with the time span of the O_4 anomaly in the time series. It took roughly 30 min to fly over the cloud system, implying that it was about 480 km wide. The enhancement in the DOAS O_4 SCDs was about 3 min long, whereas the maximum in the cloud water was observed for about 5 min (Fig. 2 18:24:00–18:29:29). The difference might be explained by a shorter light path towards the edges of the clouds. We conclude that the part of the cloud crossed was about 50–80 km wide.

3.1 Light path estimates

Inside the cloud the light path is enhanced by a factor of 3 due to the scattering on the cloud droplets. A well known tool to estimate the length of the light path is the comparison of modelled and observed O_4 column densities (e.g. Erle et al., 1995; Wagner et al., 2004; Frieß et al., 2006; Heue, 2005). We used the three-dimensional radiative transfer model McArtim (Deutschmann et al., 2011) to simulate the light propagating through the cloud to the three telescopes inside the cloud. The model enabled us to simulate a three-dimensional cloud with a base area of $150 \times 60\,km^2$ and on top of it a

ACPD
13, 24343–24403, 2013

small cloud with $50 \times 20\,km^2$. To reduce the computer time, the cloud dimensions we assumed were smaller than the real cloud.

In the simulation we focus on the estimate of the cloud extinction (CE) of the total cloud and the cloud top height (CTH) of the part the aeroplane passed through. These two parameters were varied in the range of 7 to 25 km^{-1} and 13 to 16 km, respectively. In total we simulated over 300 clouds for 3 lines of sight each. The cloud base was fixed at 1 km (based on the ECMWF model data and the video camera) and the cloud top was 9 km except for the small part that the aeroplane intersected. Because the flight altitude was 11.6 km, the minimum altitude for that part of the cloud was about 12 km. According to the ECMWF data (TRAJKS model) the mixed phase (ice and liquid water) reached from 5 to 7.5 km, therefore we assumed the water to be liquid up to 6 km and hence used an asymmetry factor of $g = 0.85$ for the water cloud and $g = 0.7$ for the ice cloud above 6 km. For both, water and ice cloud, the single scattering albedo of the cloud droplets was set to unity. The model simulates the air mass factor (AMF) for a certain altitude range (Box-AMF), which is afterwards multiplied with the local vertical column density (VCD) and co-added to retrieve the slant column density. For the comparison with the measurements the simulated O_4 column densities were interpolated by a two-dimensional (CTH and CE) second order polynomial. Also the length of the light path and the air mass factors are interpolated in the same way.

We followed the suggestions of Wagner et al. (2009) and Clémer et al. (2010) and corrected the measured O_4 SCDs with a factor of 0.8 before comparing them to the simulations. The influence of this correction is briefly discussed in Sect. 4.1 together with the uncertainty of the O_4 SCD.

The minimum difference between the measured and the calculated O_4 dSCDs should be the best approximation of the real conditions in the cloud. However, a clear global minimum was not identified (Fig. A2). Instead a local minimum for each cloud top height (CTH) between 13.4 and 17 km was found. The local minima in the deviation from the measurement for each CTH between 13.5 and 16 km (step 0.5 km) were calculated. The cloud extinction coefficient varied between 20.2 km^{-1} and 7.6 km^{-1}. The length

ACPD
13, 24343–24403, 2013

of the light path ranged from 92 km (for 13.5 km CTH and 20.2 km^{-1} CE) to 107 km (for 16 km and 7.6 km^{-1}). An overview of the estimated path length is given in Sect. 4 (Table 4) together with the retrieved mixing ratios for the different trace gases. Additional details on the comparison between the measured and the simulated O_4 column densities are described in appendix A1.

The same convective system was observed by the MODIS Aqua instrument (data available at: http://ladsweb.nascom.nasa.gov/, February 2013) at 17:20 UTC i.e. 1 h before the CARIBIC measurements. According to these data the cloud top pressure was between 120 and 105 hPa and the cloud top temperature between 197.5 and 200 K, which corresponds to a CTH of 15 to 16 km. This is comparable to our retrieved altitude range, but in the one hour period between the MODIS observation and the CARIBIC flight, the cloud may have changed. A more detailed comparison between MODIS and CARIBIC is described in the radiative transfer modelling appendix A2.

4 Trace gas concentrations in the cloud

In contrast to the insitu NO and H_2O measurements the DOAS observations average over a long light path inside the cloud. Therefore for a comparison or a combined analysis we have to assume that these measurements are representative for the rest of the cloud. Nitrogen monoxide (Fig. 2 18:24–18:29) had an average value of 1.48 ± 1 ppb (median 1.24 ppb) but showed several sharp peaks. Often such peaks are caused by air traffic (e.g. 18:13 UTC Fig. 2) with a concurrent peak in the aerosol data. Inside the cloud also lightning can produce large amounts of NO_x (e.g. Schumann and Huntrieser, 2007). In our case lightning is the most likely source of the NO peaks and the enhanced NO background as the peaks are broader than for contrails and not accompanied by a peak in the fine aerosols as often observed in contrails.

Although the DOAS observations average over a long light path (≈90. . . 100 km, Table 4), the instrument is most sensitive close to the flight altitude, where the local Box-AMF is close to 20. This means that it is roughly three times higher than in the cloud

ACPD
13, 24343–24403, 2013

free case. Nevertheless also lower parts of the cloud contribute to the signal, and are consequently considered in the light path estimate. To derive the mixing ratio of HONO, HCHO, and NO_2 we again assume a constant mixing ratio *MR* inside the cloud, which can be derived from the measurements via:

$$dSCD = MR \cdot BoxAMF_{\text{cloud}} \cdot VCD_{\text{cloud}}(air) \quad (2)$$

The product $BoxAMF_{\text{cloud}} \cdot VCD_{\text{cloud}}(air)$ depends on the cloud top height and cloud extinction coefficient. With the assumption of a constant mixing ratio its dependency on the profile is fixed. This enabled us to interpolate the simulated BoxAMF multiplied with the vertical column density of air (see O_4 SCD in Sect. 3.1), by which the variability caused by the simulation is reduced.

The approach (Eq. 2) neglects the reference SCD, which had to be added to the measured dSCD first. However, this error might be corrected if the background profile of the trace gas was known. Assuming a typical background NO_2 profile with constant mixing ratio of 20 ppt NO_2, in the altitude range of the cloud, results in a reference SCD of $\approx 1 \times 10^{15}$ molec cm^{-2}. The additional NO_2 mixing ratio in side the cloud is roughly 10 ppt. In general the correction is given by the mixing ratio multiplied with the ratio of the Box-AMFs $BoxAMF_{\text{Ref}} / BoxAMF_{\text{Cloud}}$. For the cloud's altitude range it is about half of the background mixing ratio. This correction factor is independent of the species.

In Sect. 3.1 we showed, that the interpretation of O_4 dSCD leads to an ambiguous cloud top height and cloud extinction. However, the variability in the length of light path is rather small namely ± 5 %. As expected, for the retrieved mixing ratios the differences are similar, as listed in Table 4. In general the mixing ratios decrease with increasing cloud top height. They vary around 36.7 ppt, 394.7 ppt and 171.3 ppt for HONO, HCHO, and NO_2 respectively.

The BrO detection limit of 1 ppt for nadir and +10° can be retrieved by applying the same AMF to the SCD detection limit of $6 \ldots 7 \times 10^{13}$ molec cm^{-2}. We also performed a sensitivity test artificial spectra. We added the BrO cross section multiplied with the column density and some artificial random noise to the reference and found a similar

ACPD
13, 24343–24403, 2013

value (0.8 ppt) for the detection limit as based on the retrieval error. Hence the average BrO mixing ratio in this cloud was less than 1 ppt.

4.1 Error estimates

In Table 2 the typical DOAS retrieval errors are listed for the three lines of sight and the retrieved trace gases. The errors in the retrieved mixing ratios of HONO, HCHO, and NO_2 scale linearly with the errors in the retrieved SCD i.e. if the error of the slant column density is 20 %, then the error of the mixing ratio is 20 %; only for the -10° viewing direction the error is 40 %.

The light path estimate (Sect. 3.1) is based on the retrieved O_4 SCD, hence the error in the O_4 column density (5...10 %) influences the mixing ratios of all trace gases. To estimate influence of the O_4 error on the retrieval we added ± 15 % (slight overestimation) to the retrieved column density, and compared these erroneous data to the simulated O_4 SCD. However, the influence was found to be small, for a CTH of 15 km the CE is 10.75 km^{-1} instead of 9.85 km^{-1}. The change in the mixing ratios of the other trace gases caused by this change in the O_4 SCD is listed in Table 5. Overall it can be estimated to be 2.5 ppt for HONO, 27 ppt for HCHO, and 12 ppt for NO_2. If we use the uncorrected O_4 column densities in the retrieval, the averaged mixing ratios are 33.3 ppt HONO, 357 ppt HCHO, and 155 ppt NO_2.

The statistical error caused by the Monte Carlo algorithm is 2 % as estimated by the radiative transfer model McArtim itself. The residual of the two-dimensional polynomial fit for the O_4 column densities, however was $\pm 1.50 \times 10^{42}$ $molec^2$ cm^{-5}. So the influence on the retrieved mixing ratios is of the same size as the error of the O_4 column densities. The comparison of the simulated with the measured O_4 SCD lead to an ambiguous result, which causes an uncertainty in the inferred mixing ratios of 5 % (Table 4).

Up to now we assumed a constant mixing ratio throughout the cloud (1 km to CTH). A large uncertainty, however, derives from the unknown distribution of the trace gases in the cloud. Therefore we made additional estimates using other profiles: the first one with a constant mixing ration above 8 km and zero below 8 km, for HONO a constant

ACPD
13, 24343–24403, 2013

mixing ratio in the uppermost 2 km of the cloud (12.5–14.5 km) was calculated, and for NO_2 we assumed a constant mixing ratio below 6 km and an exponential decrease (scale height 3 km) up to the cloud top. The inferred mixing ratios are listed in Table 6. While only a moderate increase (≈25 %) is found, if the mixing ratio is constant above 8 km, the HONO mixing ratios increases up to 160 ppt, if HONO is concentrated in the uppermost 2 km. The DOAS instrument is less sensitive for trace gases at lower altitudes, therefore, if most of the NO_2 is below 6 km, the same slant column density can only be explained by much higher concentrations i.e. 470 ppt below 6 km followed by the exponential decrease. All these profiles are more or less arbitrary and give a rough estimate on the variability of the possible profiles and the corresponding mixing ratios. The real profiles for the three observed trace gases are unknown and might be different from one another. According to the chemistry described in Sect. 1, different profiles for HONO and NO_2 are rather likely. Nevertheless we will use the constant mixing ratio (1...CTH) in the following for our calculation. These mixing ratios are a lower threshold (Table 6) as the concentrations can only be lower if enhanced concentrations of the respective tracers were outside the cloud (below or above).

5 Sources of the nitrogen oxides, nitrous acid and formaldehyde

To recapitulate, on the flight to Caracas on 16 August 2011 a large thunderstorm cloud was intersected. Inside the cloud NO (1.48 ppb), NO_2 (170 ppt), HONO (37 ppt) and HCHO (400 ppt) were enhanced. Next we will explore the possible sources.

Although one has to be aware of using back trajectories inside convective systems, we note that all trajectories calculated with TRAJKS originate from the east i.e. from the central Atlantic (15°...18° N, 30°...60° W). Hence the system followed the typical pathway of waves during the summer hurricane season. As a consequence no significant updraught of NO or HONO can be expected. Moreover the life time of HONO (≤ 5 min) is far too short for it to be transported over a longer distance, so that we expect the enhancement to be caused by local photochemistry. An updraught of HCHO

ACPD
13, 24343–24403, 2013

is however well possible as the marine background mixing ratios of HCHO reach up to 800 ppt (Sect. 5.3.1).

5.1 Nitrogen oxides

Both, the high variability in the NO mixing ratios and the clean air origin of the air masses lead to the conclusion, that the observed NO originated from lightning. Data from the World Wide Lightning Location Network (http://wwlln.net, March 2013) indicate strong lighting activity in this area during the hours prior to the measurement. Figure 5 shows the registered flashes in the last 3.5 h prior to the CARIBIC measurements. There had been a strong activity just east of the flight track in the last hour, which was still ongoing when our measurements took place (therefore the next 15 min are included). The distance between the flight track and the area of the strong lightning was about 0.4° (E–W) or roughly 40 km. According to the ARINC data the wind speed was roughly 18 m s^{-1} from the east (75°...80°), so the distance corresponds to a transport time of The flash density upwind of the flight track varied between 0.28 and 11.14 flashes per 100 km^2 and hour with an average of 1.8 and a median of 1.14. According to Beirle et al. (2010, Fig. 3a) the detection efficiency (DE) of the WWLLN varies between 15 and 20 % in this region. The data shown in Fig. 5 are uncorrecetd, but for the source estimate in Sect. 5.4.1 the flash density is multiplied by 5.5 (18 % DE).

Lightning is thus the likely source for the observed enhancements in the NO (1.48 ppb) and NO_2 (170 ppt) mixing ratios. A box model simulation (Sect. 5.4.1) showed, that a lightning density of ≈ 6 flashes/(100 km^2 h) is sufficient to explain the observed NO mixing ratios.

As mentioned in the introduction (Sect. 1) the Leighton ratio NO/NO_2 is important for the fate of OH. In the steady state the Leighton ratio may also be calculated via the O_3 concentration and the actinic flux. We used a modelled flux from the Tropospheric Ultraviolet and Visible (TUV) Radiation Model (quick TUV calculator http://cprm.acd.ucar.edu/Models/TUV/Interactive_TUV/, March 2013). To mimic the brightness of the cloud, a surface albedo of 1 was assumed. An ozone column of 250 DU was included,

ACPD
13, 24343–24403, 2013

based on SCIAMACHY data (www.iup.uni-bremen.de, March 2013). Compared to a clear sky scenario with a ground albedo of 5 % the actinic flux is roughly double (in the range of the results given by Brasseur et al., 2002). For comparison, the intensity measured by the DOAS spectrographs in the cloud was two to three times as high as in the reference spectrum over the Atlantic ocean.

Dividing the insitu NO measurements by the DOAS NO_2 observations results in a rather low ratio (≈8.7). Compared to the estimates (up to 27) based on a simulated flux and the measured O_3 concentrations it is a factor three lower. Hence we have to assume, that the local NO_2 concentrations are a third of our DOAS observations. The main reason might be that different air masses were observed by the NO and the DOAS instruments, because the light path of the DOAS was roughly 100 km. Moreover the actinic flux may be overestimated, especially for the lower parts of the cloud, which also contribute to the observed NO_2 SCD. The difference between the observed and estimated Leighton ratios indicates that the assumption of a constant NO_2 profile was too simple. If we use the NO_2 profile described in Sect. 4 with a constant mixing ratio up to 6 km and an exponential decrease above, the mixing ratio at flight altitude (11.6 km) is 73 ppt, which is close to the NO_2 data based on the Leighton ratio.

5.2 Nitrous acid and OH

In the previous section we showed that lightning was the dominant NO_x source. But also HONO and OH are produced with the lightning flashes (Bhetanabhotla et al., 1985). According to their simulations the OH concentration increases up to 4×10^8 molec cm^{-3} during the first millisecond after the flash. Of course the OH radical rapidly reacts with other species and is thereby destroyed, but most of these products just store the OH radical temporally e.g by conversion to HONO (Sec.1). On a longer time scale (1 sec) Bhetanabhotla et al. (1985) predicted a HONO to NO production rate by flashes of 6.7×10^{-3}. If we neglect additional sources of HONO or NO the initial HONO mixing ratios caused by lighting amount to ≈ 10 ppt HONO, based on the observed NO mixing ratio and the simulated HONO to NO ratio. After longer time periods

ACPD
13, 24343–24403, 2013

(minutes) HONO, NO and OH will reach a photo-stationary state. Despite the different air masses for HONO and NO measurements (Subsec. 5.1), we assume HONO, NO and OH to have been in photo-stationary steady state defined by the reactions R2 and R3, R4 (Sect. 1). Thereby we can estimate the OH concentration at flight altitude:

$$[\mathrm{OH}] = \frac{J_{\mathrm{R3}} \cdot [\mathrm{HONO}]}{k_{\mathrm{R2}} \cdot [\mathrm{NO}] + k_{\mathrm{R4}} \cdot [\mathrm{HONO}]} \quad (3)$$

This calculation results in an OH concentration of 1.3×10^7 molec cm^{-3} or 2 ppt at flight altitude. Because additional HONO sources (e.g. outgassing during freezing) are not considered, the OH concentration might be overestimated. Stickler et al. (2006) retrieved (1.9×10^7) molec cm^{-3} from a model and speculated that the model might overestimate the OH concentrations. We applied the same model and got roughly 4 ppt OH at flight altitude.

5.3 Formaldehyde

In the following we will try to estimate the source strength of individual potential HCHO sources i.e. updraught of boundary layer HCHO, chemical production by methane oxidation and other tracers including isoprene. In doing so, several assumptions have to be made and literature data used, yet the present study is one of few available at flight altitude. Also a simple box model is used, to estimate the photo-stationary state, based on the basic chemical reactions, this must not be mixed up with the CAABA model described in Sect. 5.4.

5.3.1 Updraught from the Boundary Layer

For the free and upper troposphere, formaldehyde mixing ratios of 500 ppt and more have been reported (e.g. Fried et al., 2008a; Klippel et al., 2011; Apel et al., 2012). Often convective transport of HCHO itself or reactive hydrocarbons are mentioned as sources. Our observations happened to take place in a strong convective system over

ACPD
13, 24343–24403, 2013

a clean marine area. Background levels of formaldehyde in the marine boundary layer are less than 1 ppb (Fried et al., 2008a), for remote regions like the central Pacific even lower values of 200 ppt were observed (Fried et al., 2003). According to the global chemistry climate model EMAC (Jöckel et al. , 2010) the 5 day average HCHO mixing ratio in the marine boundary layer around Guadeloupe in August is about 600 –800 ppt, of which 88 % are caused by methane oxidation (S. Gromov personal communication). In contrast to HCHO the marine background NO is merely ≈ 100 ppt. In the preceding Sect. 5.1 we assumed the NO updraught to be negligible, based on the background mixing ratio this is still justified, even though we assume updraught to be a major HCHO source at flight altitude.

If we assume 600 ppt HCHO for the boundary layer around Guadeloupe, a strong updraught might result in HCHO mixing ratios of up to 300 ppt inside the cloud as estimated below. The mixing ratio for soluble species Y_{conv} in a strong convection is given by:

$$Y_{conv} = (1 - SE) \cdot \beta \cdot Y_{BL} + (1 - \beta) \cdot Y_{UT}, \quad (4)$$

where Y is the mixing ratio inside the convection (conv), the boundary layer (BL) and the upper troposphere (UT), SE is the scavenging efficiency and β is the fraction of fresh boundary layer air inside the convection (formulation copied from: Borbon et al., 2012). The input from the free troposphere has to be neglected, because the knowledge about the local concentrations is too poor. We cannot calculate the parameters β and SE here, hence we rely on the data from the AMMA campaign (Borbon et al., 2012). However, there the scavenging efficiency varied between 4 % and 40 % and the fraction of boundary layer air in the UT varied between 35 % and 50 %. If the boundary layer contained 600 ppt HCHO and the UT background over the Atlantic was 50 ppt the convective air masses contained between 158 and 313 ppt, depending on the parameters β and SE. A more detailed estimate on the updraught's magnitude (43×10^{23} molec (km^{-3} h^{-1})) which also includes CH_3OOH as direct precursor is given in Sect. 5.4.

ACPD
13, 24343–24403, 2013

5.3.2 Oxidation of methane and other hydrocarbons

An obivous source of HCHO is the reaction of CH_4 with OH and subsequent reactions, in steady state:

$$[\mathrm{HCHO}] \cdot (k_9 \cdot [\mathrm{OH}] + J_1 + J_2) = k_{10} \cdot [\mathrm{OH}] \cdot [\mathrm{CH_4}] \quad (5)$$

Under background conditions (3×10^6 molec cm^{-3} of OH and photolysis rates of 0.6×10^{-4} and 0.55×10^{-4} s^{-1}) the HCHO mixing ratio is 36 ppt, comparable to 40 ppt from Fried et al. (2003) over the Pacific. For the conditions inside the cloud (1.3×10^7 molec cm^{-3} OH and the photolysis rate being doubled), a HCHO mixing ratio of 63 ppt is found. The increase is mainly caused by the higher OH concentrations (factor 4), compared to the background conditions. If ethane (400 ppt), propane (10 ppt), methylcloride (500 ppt) and acetone (300 ppt) are included in the model as additional sources, an increase of 10 ppt is found (74 ppt HCHO).

Moreover, the temporal dependence of the HCHO formation has to be considered. According to Fried et al. (2008b) it takes about one day until the HCHO formed by uplifted precursors reaches the same HCHO level as direct uplift. Using the basic mechanism, a simple box model showed that it roughly takes 3 h for the HCHO concentration to reach the new equilibrium with enhanced OH and enhanced photolysis inside the cloud. In the last 3.5 h prior to the CARIBIC lightning was observed in the region (Fig. 5). According to this, the time should be sufficient to reach equilibrium again, while ongoing lightning activity continues to change the concentrations of OH, HONO, and NO. Therefore a steady state can only be achieved for a limited time span if at all.

The methane oxidation was also included in the CAABA box-model simulation, but this source is found too weak, only 119 ppt HCHO were calculated. Therefore additional precursors such as isoprene or HCHO updraught are necessary to reach the observed HCHO mixing ratio of 400 ppt.

ACPD
13, 24343–24403, 2013

5.3.3 Isoprene

Isoprene is often mentioned as the most important formaldehyde precursor (e.g. Stickler et al., 2006; Apel et al., 2012). However, the main source of isoprene is plant emissions on land (500 Tg carbon yr^{-1}, Apel et al., 2012). Compared to that the oceanic emissions (1...10 Tg carbon yr^{-1}, Shaw et al., 2010) are almost negligible. In their review paper Shaw et al. (2010) list atmospheric marine isoprene mixing ratios between below 1 and 300 ppt, but usually below 10 ppt for the remote marine boundary layer. The higher end of this range is assumed to be influenced by coastal (land) emissions. If we include 1.4 ppt isoprene at flight altitude in the HCHO source estimate for the cloud (2 ppt OH), the steady state concentration rises from 74 ppt to 78 ppt in addition to the up-lifted HCHO. The CAABA box model (Sect. 5.4) showed that, the inclusion of isoprene emissions combined with ongoing NO emissions results in a strong formaldehyde production and the final isoprene level would be 1.4 ppt. However, updraught of isoprene in the same order of magnitude as HCHO and CH_3OOH is very unlikely, considering the background mixing ratios of less than 10 ppt for isoprene and several hundred ppt of HCHO and CH_3OOH.

5.3.4 Altitude effects

DOAS measurements average over a long light path and a wide altitude range. Up to now we assumed the HCHO and HONO mixing ratios to be constant inside the cloud and on the other hand we assumed the HCHO to be formed close to the flight altitude. Both are not necessarily true, if the formaldehyde was formed at lower altitudes this changes the reaction coefficients and at 6 km the temperature is −7 °C, so the calculations (Eq. 5) result in 79 ppt and 203 ppt, for low and high OH respectively. Here we neglected the decrease of the photolysis rate inside the cloud. Within the strong convection this enhancements may be transported to higher altitudes quickly.

ACPD
13, 24343–24403, 2013

5.3.5 Summary of first order estimates

An overview of the individual sources and their estimated contributions to the observed formaldehyde is given in Table 8. The exact origin of the observed formaldehyde enhancement cannot be identified, even though a range of additional tracers are measured with CARIBIC. Direct updraught seems to be the largest source. The oxidation of methane and acetone contribute 82 and 7 % of the chemical produced formaldehyde. The formation of HCHO based on isoprene, which showed a large impact in other studies, contributes only 5 % to the chemical formed HCHO, in our first order estimate. The methane oxidation depends on the altitude and increases at lower altitude.

5.4 CAABA box model simulations

The CAABA chemical box model was used to simulate the chemical processes within the cloud and to estimate the source strength of lightning NO and updraught HCHO. We do not expect chemical steady-state under the extreme meteorological conditions beyond a few hours, but temporary chemical regimes with very fast chemistry due to intense photolysis, HO_x and NO_x chemistry.

The longer-lived tracers with lifetimes in the order of days were fixed to their initial values to allow shorter-lived tracers to adjust accordingly in a steady state calculation. Steady state of the system was defined by a change in OH and HO_2 of less than 10^{-6} molecules/cm^3 within 15 min. Whenever NO was emitted, this definition was instead applied to NO and HONO concentrations.

Fixed species included N_2, O_2, H_2O, O_3, CO, CO_2, CH_4, N_2O, C_2H_2, C_2H_6, C_3H_8, C_4H_{10}, CH_3COCH_3, CH_3OH, and H_2. Ozone was included in the set of fixed species following Prather and Jacob (1997) and 3-D model studies that confirmed the strong influence by transport and little influence by local photochemistry (Pommereau et al., 2011). Hydrogen levels were fixed at 510 ppt, as typically observed at 16° N in the upper troposphere (Batenburg et al., 2012). Among others, the nitrogen species observed by DOAS were not fixed and free to vary according to box model conditions. For all emis-

ACPD
13, 24343–24403, 2013

sion scenarios, observed mixing ratios for VOCs like ethane, methanol, and acetone were initialized as observed in the cloud (Table 3).

In a first step a background upper troposphere atmosphere was simulated as steady state. For this the typical background measurements of CARIBIC (Table 3) were included or if not available literature data were used. Based on the median values of tracers within the cloud and whole-air sample No. 14, the initial mixing ratios of NO and NO_2 were reduced until NO equilibrated at around 150 ppt as was observed before entering the cloud. The background simulation equilibrated for 40 days to reach a stable mixing ratio for PAN (42 ppt), one of the longest-lived non-initialized tracers.

In a second step a regular input of NO was used to simulate the lightning NO emissions. Because the HCHO concentration decreased, if only NO was emitted, we additionally simulated the simultaneous updraught of HCHO or the precursors CH_3OOH or isoprene. Note that only one of these three HCHO sources was included. The included sources and the source strength, necessary to explain our results, are listed in Table 9.

Based on the model we retrieved an NO source strength of 3.2×10^9 molec cm^{-2} s^{-1} km^{-1} for the altitude range around the flight altitude, if only NO emission are considered. However, the modelled mixing ratios of HCHO and HONO were lower than the observations (initial values in Fig. 6).

In addition to the local NO mixing ratios we also wanted to understand our HCHO and HONO observations, therefore an updraught of HCHO or its precursors CH_3OOH and isoprene was simulated. The simulation of VOCs emissions only depleted the system in NO (Fig. 6) and with respect to the simulation time (Fig. 10), it took about 1 day to reach 400 ppt HCHO, probably longer than the typical turnover time in a thunderstorm. These results might be representative for strong convection without lightning (NO emissions) and agree quite well with other findings (e.g. Fried et al., 2008b).

Only a combination of lightning NO and updraught of HCHO, CH_3OOH or isoprene explains both the enhanced NO measurements and the HCHO and HONO observations. The influence of these three VOCs on the estimated NO emissions is rather small. It varies between 8.05 for NO plus isoprene, 8.2 for NO plus CH_3OOH

ACPD
13, 24343–24403, 2013

and 8.5×10^9 NO molec cm^{-2} s^{-1} km^{-1} if HCHO is emitted with the nitrogen monoxide. The source strength of HCHO, CH_3OOH or isoprene are 121, 96 and 36×10^9 molec cm^{-2} s^{-1} km^{-1}, respectively (Table 9). This confirms previous studies (e.g. Stickler et al., 2006) that isoprene in combination with NO is an effective precursor of formaldehyde. A combination of the direct HCHO updraught and the precursors is most likely. However, the partitioning between the individual sources is unknown and therefore not considered in the model. Because the estimated NO source strength is almost independent of the simulated HCHO precursor, we use an average of 8.25×10^9 NO molec cm^{-2} s^{-1} km^{-1} for the following calculations.

In Sect. 5.1 we mentioned that measured NO_2 mixing ratios were higher than the estimate based on NO and the Leighton ratio. As expected the modelled NO_2 mixing ratios agree well with this estimate and are much lower than the DOAS measurements of NO_2, which again indicates that the NO_2 profile was more complex than previously assumed.

5.4.1 Estimates of the lightning emission factor

In the following we will combine the inferred NO source strength of 8.25×10^9 molec cm^{-2} s^{-1} km^{-1} (or 2.97×10^{23} molec (km^{-3} h^{-1})) with the median flash density (6.3 flashes per 100 km^2 and hour) to estimate the lighting emission factor. First the NO source strength has to be integrated over the altitude range, because we calculated the source strength at flight altitude. The NO emission of lighting depends linearly on the pressure (laboratory studies by: Wang et al., 1998). We used the linear dependency they found and scaled it to our volume emission (8.25×10^9 molec cm^{-2} s^{-1} km^{-1}) at 205 hPa. Moreover the fractioning between intracloud (IC) and cloud to ground flashes (CG) has to be considered. The ratio of CG flashes was estimated to 6–15 % based on the CTH (13.5–16.5 km) and the freezing level (4.9 km) using the formulae cited in Pickering et al. (1998) for marine conditions. The altitude range for CG flashes typically reaches up to the −15 °C level (7.5 km) and for IC flashes it stretches from there to the

ACPD
13, 24343–24403, 2013

cloud top (Mushtak et al., 2005). For the median flash density and the pressure dependend NO emission, we calculated an NO emission factor of 4.2×10^{25} molec/flash if the cloud top height is 15 km.

The emission per flash only shows a weak dependency on the CTH i.e 3.8 or 4.6×10^{25} NO molec/flash for 13.5 and 16.5 km, respectively. The flash density on the other hand has a large impact on the estimated NO emission per flash, especially as the detection efficiency (DE) of then WWLLN has to be considered. For the previous estimate we assumed the DE=18 %, as mentioned in Sect. 5.1. The results for a large range of flash densities (Fig. 7) vary over 2 orders of magnitude depending on the flash density or the detection effiency. The most realistic values from our point of view are between 2.4 and 4.6×10^{25} NO molec/flash, based on the average or the median flash density and a DE of 18 %. In their review paper Schumann and Huntrieser (2007) listed emieeion factors in the range of 2 to 40×10^{25} NO molec/flash with an average of 15×10^{25} NO molec/flash. Our estimate is within the range though close to the lower limit.

6 Conclusions

We focused on a flight through a large thunderstorm cloud, which offered a rare opportunity. Two similar but smaller events were observed on the flight routes to Santiago de Chile (2005), and another one over southern China in 2006 (Dix et al., 2009). The DOAS instrument on the CARIBIC platform allowed an estimate of HONO (37 ppt, −8, +13 ppt), HCHO (400 ppt, −93, +136 ppt), and NO_2 (170 ppt, −42, +65 ppt). During the flight through the cloud the NO analyser measured up to 5 ppb with a mean of 1.48 ppb. Because the event was observed in the updraught of marine boundary layer air, we conclude that NO_x was caused by lightning rather than pollution.

We used the CAABA box model to estimate the NO source strength. In the model calculations combined emissions of NO and HCHO precursors showed to be essential to explain our findings. Direct HCHO updraught and CH_3OOH and isoprene as

ACPD
13, 24343–24403, 2013

precursors were considered. In these studies the necessary NO emissions varied only between 8.05 and 8.5×10^9 molecules cm^{-2} s^{-1} km^{-1}, while for the updraught of HCHO, CH_3OOH and isoprene 121, 92 and 36×10^{29} molecules cm^{-2} s^{-1} km^{-1} had to be assumed. The origin of the enhanced HCHO and HONO seems to be a combination of updraught and enhanced chemical production initiated by lightning NO_x. An emission rate of 4.2×10^{25} (2.4...4.6) NO molecules per flash is estimated based on the simulated NO emissions and the observed lightning density (World Wide Lightning Localisation Network).

Appendix A

Radiative transfer modeling

This appendix contains a more detailed description of the radiative transfer modelling inside the large cloud system the CARIBIC aeroplane crossed on the way to Caracas. A short summary of the radiative transfer modelling is given in the paper.

A1 Light path estimate

Inside the cloud the light path is extremely enhanced due to the scattering on the cloud droplets. A well known tool to estimate the length of the light path is the comparison of modelled and observed O_4 column densities (e.g. Erle et al., 1995; Wagner et al., 2004; Frieß et al., 2006; Heue, 2005). We used the three dimensional radiative transfer model McArtim (Deutschmann et al., 2011) to simulate the light propagating through the cloud to the three telescopes inside the cloud. The model enabled us to simulate a three dimensional cloud with cloud base of $150 \times 60\,km^2$ with on top of it a small cloud with $50 \times 20\,km^2$. To reduce the computer time, the cloud dimensions we assumed were smaller than the real cloud. However, for a cloud top height of 14.5 km also more realistic dimensions (400 × 400 km) were considered for the cloud extinction

ACPD
13, 24343–24403, 2013

13. . . 17 km^{-1}. The difference in the light path was about 15 %, which is in the range of the model's uncertainty. A direct comparison of the Box AMF is shown in Fig. A1.

We focussed on the centre of the cloud, where the maximum of the O_4 SCD was observed (Fig. 3). The simulation aims to estimate of the cloud's extinction coefficient and the cloud top height of the part the aeroplane passed through. These to two parameters were varied in the range of 7 to 25 km^{-1} and 13 to 16 km, respectively. The cloud base was fixed at 1 km (based on the ECMWF model data and the video camera) and the cloud top was 9 km except for the small part that the aeroplane intersected. Because the flight altitude was 11.6 km, the minimum altitude for that part of the cloud was about 12 km. According to the ECMWF data (TRAJKS model) the mixed phase (ice and liquid water) reached from 5 to 7.5 km, therefore we assumed the water to be liquid up to 6 km and hence used an asymmetry factor of $g = 0.85$ and $g = 0.7$ for the ice cloud above 6 km. For both water and ice cloud the single scattering albedo of the cloud droplets was set to unity. In total we simulated over 300 clouds for 3 lines of sight each. Depending on the computer and the cloud properties it took up to 5 days per cloud. By multiplying the square of the local O_2 concentration with respective Box-AMF and the box height the O_4 slant column density can be calculated as sum of these products. For the comparison with the measurements the simulated O_4 column densities were interpolated by a two dimensional (CTH and CE) second order polynomial. Also the length of the light path and the air mass factors are interpolated in the same way.

We followed the suggestions of Wagner et al. (2009) and Clémer et al. (2010) and corrected the measured O_4 SCDs with a factor of 0.8 before comparing them to the simulations. The influence of this correction is briefly discussed in Sect. 4.1 of the paper together with the uncertainty of the O_4 SCD.

The minimum difference between the measured and the calculated O_4 dSCDs should be the best approximation of the real conditions in the cloud. Therefore we subtracted the measurements from the simulated column densities for all viewing directions and calculated the root of the squared errors. However, a clear global minimum was not

ACPD
13, 24343–24403, 2013

identified (Fig. A2), instead a local minimum for each cloud top height (CTH) between 13.4 and 17 km was found.

For all three viewing direction a minimum deviation between measurement and simulation should be found for the same parameters of the cloud. This is only achieved by including the reference in the simulation. Directly below and to the right (viewing direction of the telescopes) no clouds were seen in the video data, but it was hazy, therefore we included a thin cirrus cloud at flight altitude (9–11 km). A reasonable but still not perfect agreement (Fig. A3) is found for a cloud extinction of 0.2 km^{-1} for the cirrus cloud. Mainly the −10° viewing direction deviated from the other two lines of sight. The difference of the simulated O_4 dSCD for −10° was independent of the simulated O_4 SCD of the cloud, because of that we are concluded, that this effect was caused by the simulated reference.

The local minima in the deviation from the measurement for each CTH between 13.5 and 16 km (step 0.5 km) were calculated. The cloud extinction coefficient varied between 20.2 km^{-1} and 7.6 km^{-1}. The length of the light path ranged from 92 km (for 13.5 km CTH and 20.2 km^{-1} CE) to 107 km (for 16 km and 7.6 km^{-1}). An overview of the estimated path length is given in Table 4 together with the retrieved mixing ratios for the different trace gases.

A2 Comparison with MODIS observation

The same convective system was observed by the MODIS Aqua instrument (data available at: http://ladsweb.nascom.nasa.gov/, February 2013) at 17:20 UTC i.e. 1 h prior to the CARIBIC measurements. According to these data the cloud top pressure was between 120 and 105 hPa and the cloud top temperature (Fig. A4) between 197.5 and 200 K, which corresponds to a CTH of 15 to 16 km, which is at the upper end of our retrieved altitude range.

The total cloud extinction for such large and optical dense clouds is not a standard product provided by the MODIS team on the internet, instead a minimum thresh-hold of 100 is given. Therefore the cloud optical thickness of the DOAS data can not be

ACPD
13, 24343–24403, 2013

compared to the MODIS analysis. Instead a comparison of the cloud effective radius (droplets) can be performed. It is calculated from the MODIS data giving a cloud effective radius of 20 to 24 µm with an error estimate ± 5 µm. The cloud effective radius r correlates the cloud water content w with the cloud extinction coefficient k according to:

$$k = 2 \cdot N \cdot \pi \cdot r^2$$

$$w = \frac{4}{3} \cdot N \cdot \pi \cdot r^3 \cdot \rho$$

Combining these two equations results in:

$$r = \frac{3 \cdot w}{2 \cdot k \cdot \rho} \quad \text{(A1)}$$

Where N is the number density of cloud droplets, and $\rho = 0.918\,\mathrm{g\,cm^{-3}}$ the ice mass density. The cloud water content w can be retrieved from the cloud water measurement. At flight altitude 948 ppm (Fig. 2) corresponds to 0.19 g water per m^3. Because the water content is almost constant (Table 3), the cloud effective radius depends on the cloud extinction k only, which is a function of the cloud top height (Fig. A2). Hence for each cloud top height a cloud effective radius can be given (Table A1). The variability in the cloud water ± 78 ppm changes the cloud effective radius by 1.8 to 3.5 µm depending on the cloud extinction.

Comparing the data on the cloud effective radius, there is a discrepancy between MODIS and CARIBIC. The effective radius based on the MODIS observation was 22 ± 6 µm, this agrees with CARIBIC data only for the cloud top height of 13.5 to 14.5 km (Table A1). On the other hand the cloud top height according to MODIS was 120 to 105 hPa i.e. 15 to 16 km. Of course, the effective radius is a critical measure especially for ice clouds, as in Eq. (A1) we assume the ice crystal to be spherical, which is hardly ever the case. Measuring the cloud top temperature and pressure, from a satellite, should be more straight forward than calculating the effective radius. Moreover, there might be a difference in the effective radii when one observes from inside

ACPD
13, 24343–24403, 2013

the cloud as compared to observing from above. Last but not least, the cloud properties may have changed in that 1 h time span between the MODIS observation and the CARIBIC measurements. We conclude that the existing discrepancy is noticeable, but not concerning, especially as the influence of CTH on the derived mixing ratios is rather small (± 5 %).

Acknowledgements. The authors wish to thank the World Wide Lightning Location Network (http://wwlln.net), a collaboration among over 50 universities and institutions, for providing the lightning location data used in this paper. The MODIS data used in this study were acquired as part of the NASA's Earth-Sun System Division and archived and distributed by the MODIS Adaptive Processing System (MODAPS). The Atmospheric chemistry group at NCAR is acknowledged for providing the Tropospheric Ultraviolet and Visible (TUV) Radiation Model online tool. Also we also thank the satellite group in Bremen for the O_3 nadir images in the internet.

We thank Lufthansa Airlines and Lufthansa Technik especially Andreas Waibel, Thomas Dauer, Sven Dankert and Detlev Hartwig and of course the CARIBIC Team for their commitment and support. The DOAS system was build and operated by the Institut für Umweltphysik of the Universität Heidelberg. Rinus Scheele is acknowledged for helping with the trajectory calculations.

CARIBIC is financially supported by the German Ministry of Education and Science (IAGOS) and by the European Commission (IGAS). We thank Frankfurt Airport for the financial support.

The service charges for this open access publication
have been covered by the Max Planck Society.

References

Atkinson, R., Baulch, D. L., Cox, R. A., Crowley, J. N., Hampson, R. F., Hynes, R. G., Jenkin, M. E., Rossi, M. J., and Troe, J.: Evaluated kinetic and photochemical data for atmospheric chemistry: Volume I – gas phase reactions of O_x, HO_x, NO_x and SO_x species, Atmos. Chem. Phys., 4, 1461–1738, doi:10.5194/acp-4-1461-2004, 2004. 24346

Atkinson, R., Baulch, D. L., Cox, R. A., Crowley, J. N., Hampson, R. F., Hynes, R. G., Jenkin, M. E., Rossi, M. J., Troe, J., and IUPAC Subcommittee: Evaluated kinetic and photochemical

data for atmospheric chemistry: Volume II – gas phase reactions of organic species, Atmos. Chem. Phys., 6, 3625–4055, doi:10.5194/acp-6-3625-2006, 2006. 24346

Apel, E. C., Olson, J. R., Crawford, J. H., Hornbrook, R. S., Hills, A. J., Cantrell, C. A., Emmons, L. K., Knapp, D. J., Hall, S., Mauldin III, R. L., Weinheimer, A. J., Fried, A., Blake, D. R., Crounse, J. D., Clair, J. M. St., Wennberg, P. O., Diskin, G. S., Fuelberg, H. E., Wisthaler, A., Mikoviny, T., Brune, W., and Riemer, D. D.: Impact of the deep convection of isoprene and other reactive trace species on radicals and ozone in the upper troposphere, Atmos. Chem. Phys., 12, 1135–1150, doi:10.5194/acp-12-1135-2012, 2012. 24362, 24365

Baker, A. K., Schuck, T. J., Šlemr, F., van Velthoven, P. F. J, Zahn A., and Brenninkmeijer, C. A. M.: Characterization of non-methane hydrocarbons in Asian summer monsoon outflow observed by the CARIBIC aircraft, Atmos. Chem. Phys. Discuss., 10, 18101–18138, doi:10.5194/acpd-10-18101-2010, 2010. 24349

Batenburg, A. M., Schuck, T. J., Baker, A. K., Zahn, A., Brenninkmeijer, C. A. M., and Röckmann, T.: The stable isotopic composition of molecular hydrogen in the tropopause region probed by the CARIBIC aircraft, Atmos. Chem. Phys., 12, 4633–4646, doi:10.5194/acp-12-4633-2012, 2012. 24366

Baumgardner, D., Brenguier, J.L., Bucholtz, A., Coe, H., DeMott, P., Garrett, T.J., Gayet, J.F., Hermann, M., Heymsfield, A., Korolev, A., Krämer, M., Petzold, A., Strapp, W., Pilewskie, P., Taylor, J., Twohy, C., Wendisch, M., Bachalo, W. and Chuang, P.: Airborne instruments to measure atmospheric aerosol particles, clouds and radiation: A cook's tour of mature and emerging technology, Atmos. Res., 102, 10–29, doi:10.1016/j.atmosres.2011.06.021, 2011. 24353

Beirle, S., Huntrieser, H., and Wagner, T.: Direct satellite observation of lightning-produced NO_x, Atmos. Chem. Phys., 10, 10965–10986, doi:10.5194/acp-10-10965-2010, 2010. 24360

Bhetanabhotla, M. N., Crowell, B. A., Coucouvinos, A., Hill, R. D., and Rinker, R. G.: Simulation of trace species production by lightning and corona discharge in moist air, Atmos. Environ., 19, 1391–1397, 1985. 24347, 24361

Borbon, A., Ruiz, M., Bechara, J., Aumont, B., Chong, M., Huntrieser, H., Mari, C., Reeves, C. E., Scialom, G., Hamburger, T., Stark, H., Afif, C., Jambert, C., Mills, G., Schlager, H., and Perros, P. E.: Transport and chemistry of formaldehyde by mesoscale convective systems in West Africa during AMMA 2006, J. Geophys. Res. Atmos., 117, D12301, doi:10.1029/2011JD017121, 2012. 24363

ACPD
13, 24343–24403, 2013

Bogumil, K., Orphal, J., Homann, T., Voigt, S., Spietz, P., Fleischmann, O. C., Vogel, A., Hartmann, M., Bovensmann, H., Frerik, J., and Burrows, J. P.: Measurements of Molecular Absorption Spectra with the SCIAMACHY Pre-Flight Model: Instrument Characterization and Reference Data for Atmospheric Remote-Sensing in the 230–2380 nm Region J. Photoch. Photobio. A, 157, 167–184, doi:10.1016/s1010-6030(03)00062-5, 2003. 24382

Brasseur, A. L., Ramaroson, R., Delannoy, A., Skamarock, W., and Barth, M.: Three-Dimensional Calculation of Photolysis Frequencies in the Presence of Clouds and Impact on Photochemistry, J. Atmos. Chem., 41, 211–237, doi:10.1023/A:1014952630482, 2002. 24346, 24361

Brenninkmeijer, C. A. M., Crutzen, P., Boumard, F., Dauer, T., Dix, B., Ebinghaus, R., Filippi, D., Fischer, H., Franke, H., Frieß, U., Heintzenberg, J., Helleis, F., Hermann, M., Kock, H. H., Koeppel, C., Lelieveld, J., Leuenberger, M., Martinsson, B. G., Miemczyk, S., Moret, H. P., Nguyen, H. N., Nyfeler, P., Oram, D., O'Sullivan, D., Penkett, S., Platt, U., Pupek, M., Ramonet, M., Randa, B., Reichelt, M., Rhee, T. S., Rohwer, J., Rosenfeld, K., Scharffe, D., Schlager, H., Schumann, U., Šlemr, F., Sprung, D., Stock, P., Thaler, R., Valentino, F., van Velthoven, P., Waibel, A., Wandel, A., Waschitschek, K., Wiedensohler, A., Xueref-Remy, I., Zahn, A., Zech, U., and Ziereis, H.: Civil Aircraft for the regular investigation of the atmosphere based on an instrumented container: The new CARIBIC system, Atmos. Chem. Phys., 7, 4953–4976, doi:10.5194/acp-7-4953-2007, 2007. 24349, 24350

Bussemer, M.: Der Ring-Effekt: Ursachen und Einfluß auf die Messung stratosphärischer Spurenstoffe, diploma thesis, in german, Universität Heidelberg, Germany, 1993. 24382

Carter, W. P. L.; Atkinson, R.: Development and Evaluation of a Detailed Mechanism for the Atmospheric Reactions of Isoprene and NO_x, Int. J. Chem. Kinet. 28, 497–530, 1996. 24347

Clémer, K., van Roozendael, M., Fayt, C., Hendrick, F., Hermans, C., Pinardi, G., Spurr, R., Wang, P., and De Maziére, M., Multiple wavelength retrieval of tropospheric aerosol optical properties from MAXDOAS measurements in Beijing, Atmos. Meas. Tech., 3, 863–878, doi:10.5194/amt-3-863-2010, 2010. 24355, 24371

Deutschmann, T., Beirle, S., Frieß, U., Grzegorski, M., Kern, C., Kritten, L., Platt, U., Prados-Román, C., Puķīte, J., Wagner, T., Werner, B., and Pfeilsticker, K.: The Monte Carlo atmospheric radiative transfer model McArtim: Introduction and validation of Jacobians and 3D features, J. Quant. Spectrosc. Radiat. Transf., 112, 1119–1137, doi:10.1016/j.jqsrt.2010.12.009, 2011. 24351, 24354, 24370

ACPD
13, 24343–24403, 2013

Dix, B.: Spectroscopic Measurements of Atmospheric Trace Gases on Long-Distance Flights, Ph.D. thesis, Universität Heidelberg, Germany http://www.ub.uni-heidelberg.de/archiv/8118 (last access: 12 September 2013), 2007. 24347

Dix, B., Brenninkmeijer, C. A. M., Frieß, U., Wagner, T., and Platt, U.: Airborne multi-axis DOAS measurements of atmospheric trace gases on CARIBIC long-distance flights, Atmos. Meas. Tech., 2, 639–652, doi:10.5194/amt-2-639-2009, 2009. 24347, 24348, 24350, 24369

Ekman, A. M. L., Wang, C., Ström, J., and Krejci, R.: Explicit Simulation of Aerosol Physics in a Cloud-Resolving Model: Aerosol Transport and Processing in the Free Troposphere, J. Atmos. Sci., 63, 682–696, doi:10.1175/JAS3645.1, 2006. 24353

Erle, F., Pfeilsticker, K., and Platt, U.: On the influence of tropospheric clouds on zenith-scattered-light measurements of stratospheric species, Geophys. Res. Lett., 22, 2725–2728, doi:10.1029/95gl02789, 1995 24354, 24370

Fried, A., Crawford, J., Olson, J., Walega, J., Potter, W., Wert, B., Jordan, C., Anderson, B., Shetter, R., Lefer, B., Blake, D., Blake, N., Meinardi, S., Heikes, B., O'Sullivan, D., Snow, J., Fuelberg, H., Kiley, C. M., Sandholm, S., Tan, D., Sachse, G., Singh, H., Faloona, I., Harward, C. N., and Carmichael, G. R.: Airborne tunable diode laser measurements of formaldehyde during TRACE-P: Distributions and box model comparisons, J. Geophys. Res. Atmos., 108, 8798, doi:10.1029/2003JD003451, 2003. 24347, 24363, 24364

Fried, A., Walega, J. G., Olson, J. R., Crawford, J. H., Chen, G., Weibring, P., Richter, D., Roller, C., Tittel, F. K., Heikes, B. G., Snow, J. A., Shen, H., O'Sullivan, D. W., Porter, M., Fuelberg, H., Halland, J., and Millet, D. B.: Formaldehyde over North America and the North Atlantic during the summer 2004 INTEX campaign: Methods, observed distributions, and measurement-model comparisons, J. Geophys. Res. Atmos., 113, D10302, doi:10.1029/2007JD009185, 2008a. 24362, 24363

Fried, A., Olson, J. R., Walega, J. G., Crawford, J. H., Chen, G., Weibring, P., Richter, D., Roller, C., Tittel, F., Porter, M., Fuelberg, H., Halland, J., Bertram, T. H., Cohen, R. C., Pickering, K., Heikes, B. G., Snow, J. A., Shen, H., O'Sullivan, D. W., Brune, W. H., Ren, X., Blake, D. R., Blake, N., Sachse, G., Diskin, G. S., Podolske, J., Vay, S. A., Shetter, R. E., Hall, S. R., Anderson, B. E., Thornhill, L., Clarke, A. D., McNaughton, C. S., Singh, H. B., Avery, M. A., Huey, G., Kim, S., and Millet, D. B.: Role of convection in redistributing formaldehyde to the upper troposphere over North America and the North Atlantic during the summer 2004 INTEX campaign, J. Geophys. Res. Atmos., 113, D17306, doi:10.1029/2007JD009760, 2008b. 24364, 24367

ACPD
13, 24343–24403, 2013

Frieß, U., Monks, P. S., Remedios, J. J., Rozanov, A., Sinreich, R., Wagner, T., and Platt, U.: MAX-DOAS O_4 measurements: A new technique to derive information on atmospheric aerosols: 2. Modelling studies, J. Geophys. Res., 111, D14203, doi:10.1029/2005JD006618, 2006. 24354, 24370

Heue, K.-P.: Airborne Multi AXes DOAS instrument and measurements of two dimensional trace gas distribution, Ph.D. thesis, Universität Heidelberg, Germany http://www.ub.uni-heidelberg.de/archiv/5990 (last access: 12 September 2013), 2005. 24354, 24370

Heue, K.-P., Brenninkmeijer, C. A. M., Wagner, T., Mies, K., Dix, B., Frieß, U., Martinsson, B. G., Šlemr, F., and van Velthoven P. F. J.: Observations of the 2008 Kasatochi volcanic SO_2 plume by CARIBIC aircraft DOAS and the GOME-2 satellite. Atmos. Chem. Phys., 10, 4699–4713, doi:10.5194/acp-10-4699-2010, 2010. 24350

Huntrieser, H., Schlager, H., Lichtenstern, M., Roiger, A., Stock, P., Minikin, A., Höller, H., Schmidt, K., Betz, H.-D., Allen, G., Viciani, S., Ulanovsky, A., Ravegnani, F., and Brunner, D.: NO_x production by lightning in Hector: first airborne measurements during SCOUT-O3/ACTIVE, Atmos. Chem. Phys., 9, 8377–8412, doi:10.5194/acp-9-8377-2009, 2009. 24347

Jöckel, P., Kerkweg, A., Pozzer, A., Sander, R., Tost, H., Riede, H., Baumgaertner, A., Gromov, S., and Kern, B.: Development cycle 2 of the Modular Earth Submodel System (MESSy2), Geos. Mod. Dev., 3, 717–752, doi:10.5194/gmd-3-717-2010, 2010. 24363

Jurkat, T., Voigt, C., Arnold, F., Schlager, H., Kleffmann, J., Aufmhoff, H., Schauble, D., Schaefer, M., and Schumann, U.: Measurements of HONO, NO, NO_y and SO_2 in aircraft exhaust plumes at cruise, Geophys. Res. Lett., 38, doi:10.1029/2011gl046884, 2011. 24347

Klippel, T., Fischer, H., Bozem, H., Lawrence, M. G., Butler, T., Jöckel, P., Tost, H., Martinez, M., Harder, H., Regelin, E., Sander, R., Schiller, C. L., Stickler, A., and Lelieveld, J.: Distribution of hydrogen peroxide and formaldehyde over Central Europe during the HOOVER project, Atmos. Chem. Phys., 11, 4391–4410, doi:10.5194/acp-11-4391-2011, 2011. 24362

Kraus, S.: DOASIS – A Framework Design for DOAS, Shaker, 2006. 24382

Meller, R. and G. K. Moortgat (2000) Temperature dependence of the absorption cross sections of formaldehyde between 223 and 323 K in the wavelength range 225–375 nm, J. Geophys. Res., 105, 7089–7101, 2000. 24382

Mushtak, V. C., Williams, E. R., and Boccippio, D. J.: Latitudinal variations of cloud base height and lightning parameters in the tropics, Atmos. Res., 76, 222–230, doi:10.1016/j.atmosres.2004.11.010, 2005. 24369

ACPD
13, 24343–24403, 2013

Nguyen, H. N., Gudmundsson, A., and Martinsson, B. G.: Design and calibration of a multi-channel aerosol sampler for tropopause region studies from the CARIBIC platform, Aerosol Sci. Technol., 40, 649–655, doi:10.1080/02786820600767807, 2006. 24349

Pickering, K. E., Wang, Y., Tao, W.-K., Price, C., and Müller, J.-F.: Vertical distributions of lightning NOx for use in regional and global chemical transport models, J. Geophys. Res. Atmos., 103, 31203–31216, doi:10.1029/98JD02651, 1998. 24368

Platt, U., Perner, D., Harris, G. W., Winer, A. M., and Pitts, J. N.: Observations of nitrous acid in an urban atmosphere by optical absorption, Nature, 285, 312–314, doi:10.1038/285312a0, 1980. 24345

Platt, U. and Stutz, J.: Differential Optical Absorption Spectroscopy, Principles and Applications, Springer Berlin Heidelberg, 287–377, 2008. 24350

Pommereau, J.-P., Garnier, A., Held, G., Gomes, A. M., Goutail, F., Durry, G., Borchi, F., Hauchecorne, A., Montoux, N., Cocquerez, P., Letrenne, G., Vial, F., Hertzog, A., Legras, B., Pisso, I., Pyle, J. A., Harris, N. R. P., Jones, R. L., Robinson, A. D., Hansford, G., Eden, L., Gardiner, T., Swann, N., Knudsen, B., Larsen, N., Nielsen, J. K., Christensen, T., Cairo, F., Fierli, F., Pirre, M., Marécal, V., Huret, N., Rivière, E. D., Coe, H., Grosvenor, D., Edvarsen, K., Di Donfrancesco, G., Ricaud, P., Berthelier, J.-J., Godefroy, M., Seran, E., Longo, K., and Freitas, S.: An overview of the HIBISCUS campaign, Atmos. Chem. Phys., 11, 2309–2339, doi:10.5194/acp-11-2309-2011, 2011. 24366

Prather, M. J. and Jacob, D. J.: A persistent imbalance in HOx and NOx photochemistry of the upper troposphere driven by deep tropical convection, Geophys. Res. Lett., 24, 3189–3192, doi:10.1029/97GL03027, 1997. 24366

Sander, R., Baumgaertner, A., Gromov, S., Harder, H., Jöckel, P., Kerkweg, A., Kubistin, D., Regelin, E., Riede, H., Sandu, A., Taraborrelli, D., Tost, H., and Xie, Z.-Q.: The atmospheric chemistry box model CAABA/MECCA-3.0, Geosci. Model Dev., 4, 373–380, doi:10.5194/gmd-4-373-2011, 2011. 24352

Scheele, M. P., Siegmund, P. C., and van Velthoven, P. F. J.: Sensitivity of trajectories to data resolution and its dependence on the starting point: in or outside a tropopause fold, Meteorol. Appl., 3, 267–273, 1996. 24349

Schuck, T. J., Brenninkmeijer, C. A. M., Šlemr, F., Xueref-Remy, I., and Zahn, A.: Greenhouse gas analysis of air samples collected on board the CARIBIC passenger aircraft, Atmos. Meas. Tech., 2, 449–464, doi:10.5194/amt-2-449-2009, 2009. 24349

ACPD
13, 24343–24403, 2013

Schumann, U. and Huntrieser, H.: The global lightning-induced nitrogen oxides source, Atmos. Chem. Phys., 7, 3823–3907, doi:10.5194/acp-7-3823-2007, 2007. 24356, 24369

Shaw, S. L., Gantt, B., and Meskhidze, N.: Production and Emissions of Marine Isoprene and Monoterpenes: A Review, Adv. Meteorol., 408696, doi:10.1155/2010/408696, 2010. 24365

Stickler, A., Fischer, H., Williams, J., de Reus, M., Sander, R., Lawrence, M. G., Crowley, J. N., and Lelieveld, J.: Influence of summertime deep convection on formaldehyde in the middle and upper troposphere over Europe, J. Geophys. Res., 111, D14308, doi:10.1029/2005JD007001, 2006. 24347, 24362, 24365, 24368

Stohl, A., Haimberger, L., Scheele, M. P., and Wernli, H.: An intercomparison of results from three trajectory models, Meteorol. Appl., 8, 127–135, 2001. 24349

Stutz, J., Kim, E. S., Platt, U., Bruno, P., Perrino, C., and Febo, A. UV-visible absorption cross sections of nitrous acid, J. Geophys. Res. 105, 14585–14592, doi:10.1029/2000JD900003, 2000. 24382

Vandaele, A. C., Hermans, C., Simon, P., C., Van Roozendael, M., Guilmot, J. M., Carleer, M., and Colin, R.: Fourier transform measurement of NO_2 absorption cross section in the visible range at room temperature, J. Atmos. Chem., 25, 289–305, 1996. 24382

Vogel, L., Sihler, H., Lampel, J., Wagner, T., and Platt, U.: Retrieval interval mapping: a tool to visualize the impact of the spectral retrieval range on differential optical absorption spectroscopy evaluations, Atmos. Meas. Tech., 6, 275–299, doi:10.5194/amt-6-275-2013, 2013. 24351

Wagner, T., Dix, B., von Friedeburg, C., Frieß, U., Sanghavi, S., Sinreich, R., and Platt, U.: MAX-DOAS O_4 measurements: A new technique to derive information on atmospheric aerosols – Principles and information content, J. Geophys. Res., 109, D22205, doi:10.1029/2004JD004904, 2004. 24354, 24370

Wagner, T., Beirle, S., and Deutschmann, T.: Three-dimensional simulation of the Ring effect in observations of scattered sun light using Monte Carlo radiative transfer models, Atmos. Meas. Tech., 2, 113–124, doi:10.5194/amt-2-113-2009, 2009. 24355, 24371, 24382

Walter, D., Heue, K.-P., Rauthe-Schöch, A., Brenninkmeijer, C. A. M., Lamsal, L. N., Krotkov, N. A., and Platt, U.: Flux calculation using CARIBIC DOAS aircraft measurements: SO_2 emission of Norilsk, J. Geophys. Res., 117, D11305, doi:10.1029/2011JD017335, 2012. 24350

Wang, Y., DeSilva, A. W., Goldenbaum, G. C., and Dickerson, R. R.: Nitric oxide production by simulated lightning: Dependence on current, energy, and pressure, J. Geophys. Res. Atmos., 103, 19149–19159, doi:10.1029/98JD01356, 1998. 24368

ACPD
13, 24343–24403, 2013

Wilmouth, D. M., Hanisco, T. F., Donahue, N. M., and Anderson, J. G.: Fourier transform ultraviolet spectroscopy of the A 2Π3/2 ← X 2Π3/2 transition of BrO, J. Phys. Chem. A 103, 8935–8945, 1999. 24382

Zhang, N., Zhou, X., Shepson, P. B., Gao, H., Alaghmand, M., and Stirm, B.: Aircraft measurement of HONO vertical profiles over a forested region, Geophys. Res. Lett., 36, L15820, doi:10.1029/2009GL038999, 2009. 24347

Ziereis, H., Schlager, H., Schulte, P., van Velthoven, P. F. J., and Šlemr, F.: Distributions of NO, NO_x, and NO_y in the upper troposphere and lower stratosphere between 28° and 61° N during POLINAT 2, J. Geophys. Res., 105, 3653–3664, 2000. 24350

ACPD
13, 24343–24403, 2013

Table 1. Cross sections used in the DOAS retrieval.

Reference spectrum	reference
NO_2	Vandaele et al. (1996)
HCHO	Meller and Moortgat (2000)
HONO	Stutz et al. (2000)
O_4	http://spectrolab.aeronomie.be/o2.htm
O_3	Bogumil et al. (2003) (223 K and 243 K)
BrO	Wilmouth et al. (1999) (228 K)
Ring	Bussemer (1993); Kraus (2006)
Ring2	Wagner et al. (2009) (Ring·λ^4)

ACPD
13, 24343–24403, 2013

Table 2. Typical fit errors for slant column densities inside the cloud. Because the intensity in the −10° spectrograph was lower the typical fit errors are higher compared to the other two spectrographs. The BrO fit error is included here to estimate the detection limit for bromine monoxide inside the cloud.

	NO_2 $[10^{15}]$	HCHO $[10^{15}]$	HONO $[10^{14}]$	BrO $[10^{13}]$	O_4 $[10^{41}]$
	molec cm^{-2}				molec^2 cm^{-5}
+10°	1...2	5...6	5...6	3	6
−10°	3	10...12	10...12	6	12
Nadir	1...2	5...6	5...6	3	6

ACPD
13, 24343–24403, 2013

Table 3. Overview of several CARIBIC in situ measurements inside (18:24:00. . . 18:29:29) and outside (18:50. . . 19:00) the cloud. Air sample No 14 was taken at 18:31:02, which was close to the cloud edge. For comparison the values of the two previous samples (No. 12 at 17:14:57 and No. 13 at 17:52:57) are listed, as no sample was taken during the background period. Therefore the in situ methane measurements cannot be expected to agree with the samples.

Trace gas	background 18:50. . . 19:00		inside the cloud 18:24:00. . . 18:29:29
NO [ppt]	313 ± 42		1480 ± 1080
O_3 [ppb]	44 ± 0.5		35 ± 5
CO [ppb]	73 ± 0.9		73 ± 0.9
CO_2 [ppb]	391.8 ± 7.2		395.3 ± 6
Methane [ppb]	1810 ± 1.3		1807 ± 1.5
Acetone [ppt]	300 ± 100		300 ± 100
Methanol [ppt]	1058 ± 245		950 ± 213
samples	No. 12	No. 13	No. 14
Methane [ppb]	1814	1816	1806
Ethane [ppt]	653.6	790	400
Propane [ppt]	44.9	87.7	10.7
n-Butane [ppt]	2.07	5.06	1.85
Methyl chloride [ppt]	645.7	642.7	604.1

ACPD
13, 24343–24403, 2013

Table 4. Length of the light path and averaged mixing ratios of HONO, HCHO, and NO_2 inside the cloud.

CTH km	CE km^{-1}	light path km	HONO ppt	HCHO ppt	NO_2 ppt
13.5	20.2	92.1	38.4	412.3	178.9
14	14.4	94.4	39.0	419.4	182.0
14.5	11.65	97	37.9	407.3	176.8
15	9.85	99.8	36.3	390.4	169.4
15.5	8.55	103.0	34.9	375.0	162.7
16	7.6	106.8	33.9	363.7	157.8

ACPD
13, 24343–24403, 2013

Table 5. Cloud extinction coefficient for O_4 SCD errors of −15 % and +15 %, and the according range of mixing ratios for HONO, HCHO, and NO_2. For comparison the extinction coefficient for the uncorrected O_4 SCD is given. For a CTH of 13.5 km, the cloud extinction is out of the range of the simulations, therefore NO values are given also for the respective mixing ratios.

CTH	CE	CE (−15 %)	CE (+15 %)	CE (uncorrected)	HONO	HCHO	NO_2
km	km^{-1}	km^{-1}	km^{-1}	km^{-1}	ppt	ppt	ppt
13.5	20.2	17.35	> 25	> 25	< 41.9	< 449.9	< 195.3
14	14.4	13.05	16	17.2	36.2–41.8	389.0–449.2	168.8–195.0
14.5	11.65	10.6	12.75	13.55	35.5–40.4	381.3–434.5	165.5–188.6
15	9.85	8.95	10.75	11.4	34.2–38.6	367.0–415.4	159.3–180.3
15.5	8.55	7.75	9.35	9.9	32.9–37.0	353.3–398.0	153.3–172.8
16	7.6	6.9	8.3	8.8	32.1–35.7	344.4–384.1	149.4–166.7

ACPD
13, 24343–24403, 2013

Table 6. Influence of the profile shape on the retrieved mixing ratios. For the NO_2 profile the constant mixing ratio below 8 km is given.

profile shape	HONO [ppt]	HCHO [ppt]	NO_2 [ppt]
constant mixing ratio (1...CTH)	36.7	394.7	171.3
constant mixing ratio (8...CTH)	46.5	499	216
top most 2 km (12.5...14.5 km)	160		
constant exp(−z/3) ($z > 6$ km)			470

ACPD
13, 24343–24403, 2013

Table 7. Overview of different error sources and the influence on the retrieved mixing ratios.

Error [ppt]	HONO	HCHO	NO_2
Calculated values	36.7	394.7	171.3
DOAS retrieval	± 7	± 80	± 35
O_4 SCD	± 2.5	± 27	± 12
CTH-CE	± 1.9	± 28	± 16
Simulation	± 2.5	± 27	± 12
Profile (8 km. . . CTH)	+10	+100	+50

ACPD
13, 24343–24403, 2013

Table 8. Formaldehyde steady state mixing ratio [ppt] based on different input parameters. In the first column the additional parameters included are listed. For the OH concentration we used 3×10^6 molec cm^{-3} or the value retrieved in equation 3 i.e. 1.3×10^7 molec cm^{-3} for 11.6 km and 1.06×10^7 molec cm^{-3} for 6 km.

OH (cm^{-3})	3×10^6	1.3×10^7
observation	400 ppt (−93 +136 ppt)	
updraught	158...313	
CH_4, OH, J (at 11.6 km)	36 (J/2)	63
+ C_2H_6, C_3H_8, CH_3Br, acetone,	29	74
+ isoprene	31	78
no isoprene at 6 km	79	203
+ isoprene	80	206

ACPD
13, 24343–24403, 2013

Table 9. Box model emission scenarios. The emissions were adjusted to the measurements, for NO a level of 1.3 ppb was reached and for HCHO the local mixing ratio was 400 ppt. In the model the box height was fixed to 1 km, therefore the emissions to the modelled volume had the unit "molec cm^{-2} s^{-1} km^{-1}".

Scenario (emitted species)	emissions (10^9 molec cm^{-2} s^{-1} km^{-1}) NO	HCHO	CH_3OOH	isoprene
2 NO	3.2	–	–	–
3 HCHO	–	80	–	–
4 CH_3OOH	–	–	68	–
5 isoprene	–	–	–	40.1
6 NO + HCHO	8.5	121	–	–
7'NO + CH_3OOH	8.2	–	92	–
8 NO + isoprene	8.05	–	–	36.1

ACPD
13, 24343–24403, 2013

Table 10. Overview of CAABA box model results for the emission scenarios listed in Table 9. The mixing ratios are given in ppt ≡ 10^{-12} mol/mol. The unit of emission is due to an assumed box height of 1 km in the box model. Simulation time (sim. time) is given in days (d) or hours (h) until a (temporary) steady state is reached. The background simulation was running for 40 days to allow peroxyacetyl nitrate (PAN) to adapt from zero to the present conditions. Emitting isoprene alone lets H_2O_2 values unrealistically increase (not shown) also isoprene levels are unrealistic high, not so together with NO.

Scenario (emitted species)	mixing ratios (ppt) NO	HONO	NO_2	HCHO	CH_3OOH	OH	HO_2	PAN	isoprene	sim. time
1 background	153	1.4	10.5	56	14.0	1.1	10.8	41	–	40 d
2 NO	1317	33.5	60.3	119	0.6	3.0	4.0	41	–	12 h
3 HCHO	101	1.2	12.7	399	56.2	1.4	29.2	46	–	21 h
4 CH_3OOH	81	0.7	13.0	398	1606	1.0	33.6	49	–	31 h
5 isoprene	2.4	0.0	0.5	397	1225	0.02	22.3	206	3500	11 d
6 NO + HCHO	1316	53.5	74.8	401	1.3	4.7	7.5	42	–	6 h
7 NO + CH_3OOH	1316	50.6	80.0	400	403	4.5	8.1	42	–	7 h
8 NO + isoprene	1316	41.9	81.3	401	2.5	3.8	7.6	72	1.4	7 h

ACPD
13, 24343–24403, 2013

Table A1. Cloud effective radius as a function of cloud top height or cloud extinction. Here we calculated with a constant cloud water content of 948 ppm. Changing the water content by ± 78 ppm did not influence the effective radius significantly, the results are given as Δr_{eff}.

CTH [km]	13.5	14	14.5	15	15.5	16
CE [km^{-1}]	20.2	14.4	11.65	9.85	8.55	7.6
r_{eff} [µm]	15.3	21.5	26.6	31.5	36.2	40.8
Δr_{eff} [µm]	1.3	1.8	2.2	2.6	3.0	3.4

ACPD
13, 24343–24403, 2013

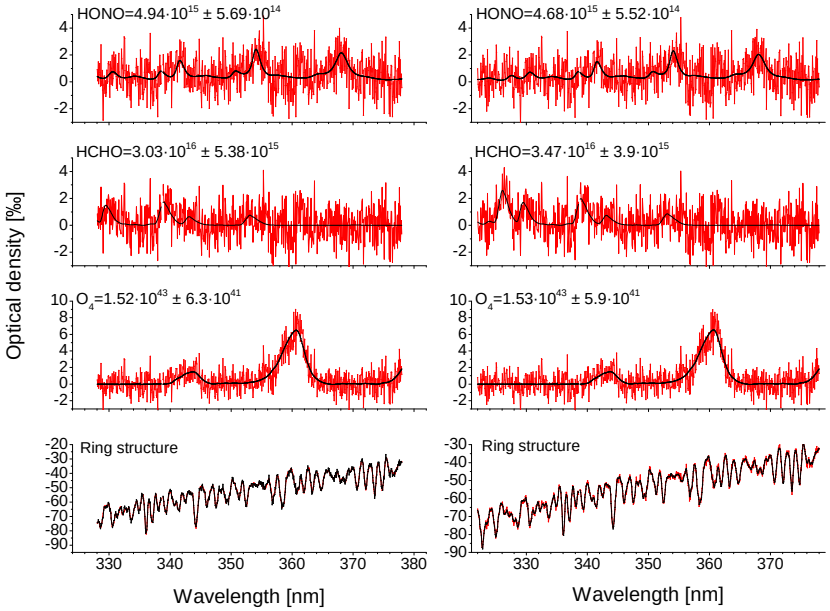

Fig. 1. Example fits using two different wavelength ranges for spectrum C0004375 (18:27:04 UTC inside the cloud) of the nadir spectrometer. For each absorber the slant column density is given next to the name. As the fit coefficient of the ring spectrum is irrelevant for the rest of the paper it is omitted here. Left the standard fitting window is used (328. . . 375 nm), right an extended range beginning at 322 nm is shown to include another HCHO absorption band. Within the error margins the results of both fits agree quite well.

ACPD
13, 24343–24403, 2013

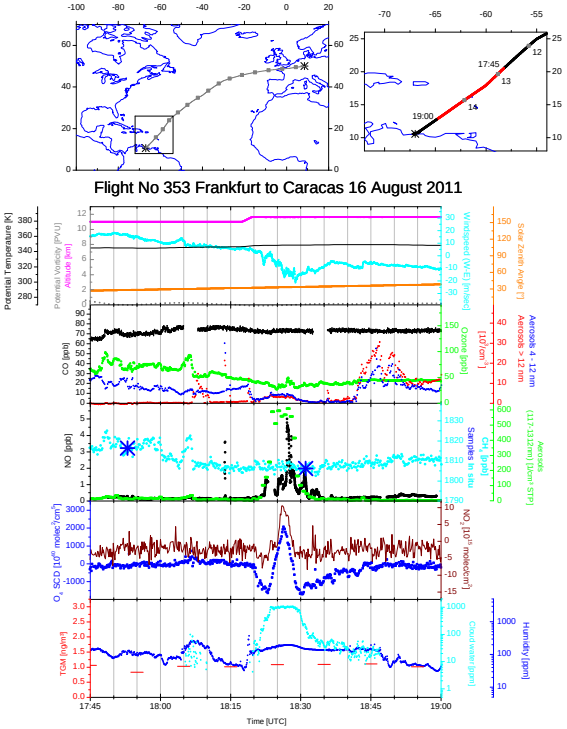

Fig. 2. Overview in selected CARIBIC measurements around the cloud (18:25 UTC). On top a map with the complete flight is shown. The box illustrates the area of the zoomed map, where the part of the flight track between 17:45 and 19:00 UTC (Table 3) is shown in red and the position of the last three air samples (12, 13, 14) is shown. The cloud is recorded by the cloud water data (lowermost panel). Concomitantly also NO and the DOAS data show some interesting features. The strong variability of NO might be attributed to lightning activity in the cloud system. For the DOAS (O_4 and NO_2) the nadir data are shown here.

ACPD
13, 24343–24403, 2013

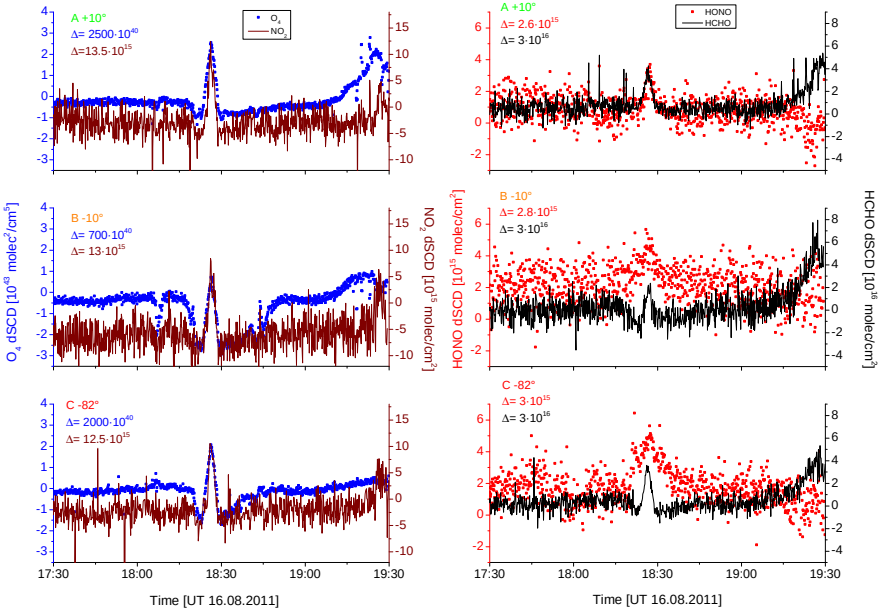

Fig. 3. DOAS data for O_4, NO_2, HONO, and HCHO (from left to right) for the three lines of sight, +10° (top), -10° (middle) and nadir (bottom). When flying through the cloud a strong increase in all these time series is observed. Especially for the downward looking telescopes the O_4 column densities are reduced relative to the back ground, while the aeroplane flies over the cloud. The difference between the background level and the enhancement inside the cloud is given as ΔSCD in the figures.

ACPD
13, 24343–24403, 2013

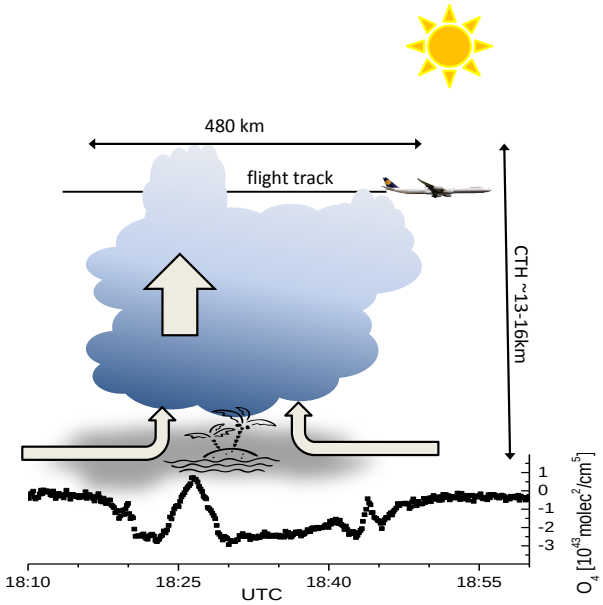

Fig. 4. Sketch of the cloud system, the CARIBIC aeroplane flew over and passed through. The width of the total cloud as well as the small part the aeroplane passed through is estimated based on the time series of the -10° O_4 SCD, which is shown below the cloud. The rest of the sketch is arbitrary. The arrows indicate the air masses flowing into the cloud and upwards inside.

ACPD
13, 24343–24403, 2013

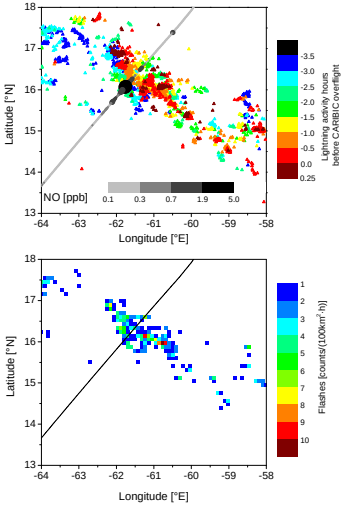

Fig. 5. Top: Flashes (one point per registered flash) according to World Wide Lightning Location Network (http://wwlln.net) colour coded with the time difference to the CARIBIC overflight (18:26 UTC). To illustrate the ongoing activity also the next 15 min after CARIBIC penetrated the cloud are included. The grey line illustrates the CARIBIC flight track colour coded with the 10 sond averaged NO data. The maximum NO is observed on the edge (south-west) of the lightning activity area. Bottom: Flash density in flashes per 100 km^2 and hour for the last 3.5 h prior to the CARIBIC overpass. The detection efficiency of 18 % is not considered here.

ACPD
13, 24343–24403, 2013

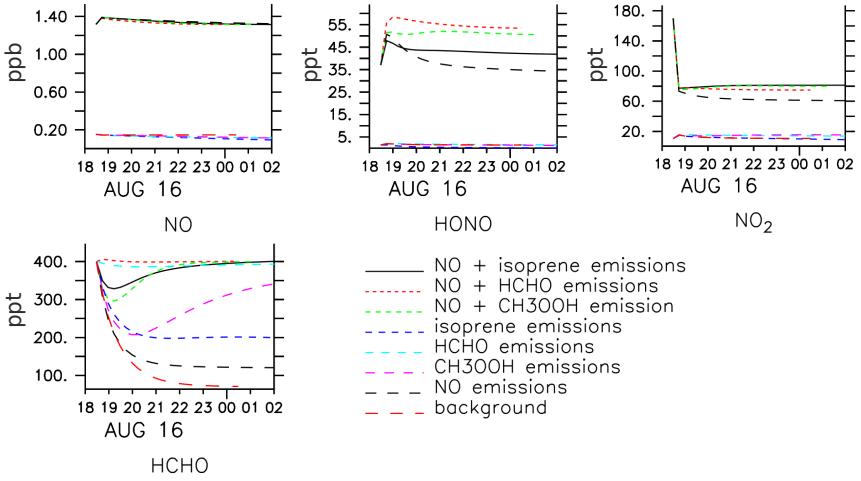

Fig. 6. Simulated mixing ratios of NO, HONO, NO_2 and HCHO as function of time for several emission (updraught) scenarios. The figure clearly shows that neither emission of NO nor HCHO only can explain the observed HONO levels, hence in the cloud the combination of lightning NO emissions and HCHO updraught lead to the formation of nitrous acid.

ACPD
13, 24343–24403, 2013

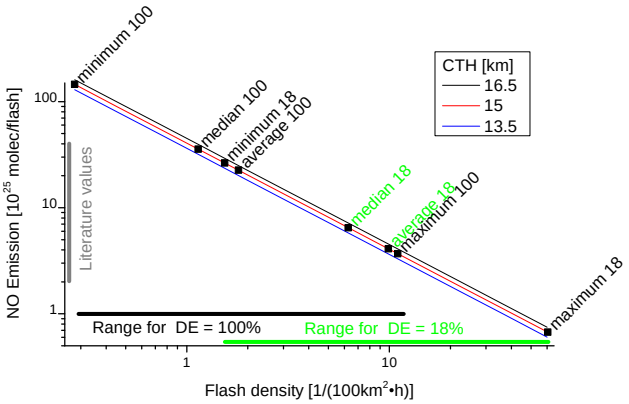

Fig. 7. NO emissions per flash, depending on the flash density and the cloud top height. The emissions necessary to explain our finding vary between 0.4 and 103×10^{25} NO molec/flash. However, these extreme values are retrieved using the minimum and the maximum flash density and assuming a DE of 100 % for the minimum flash rate.

ACPD
13, 24343–24403, 2013

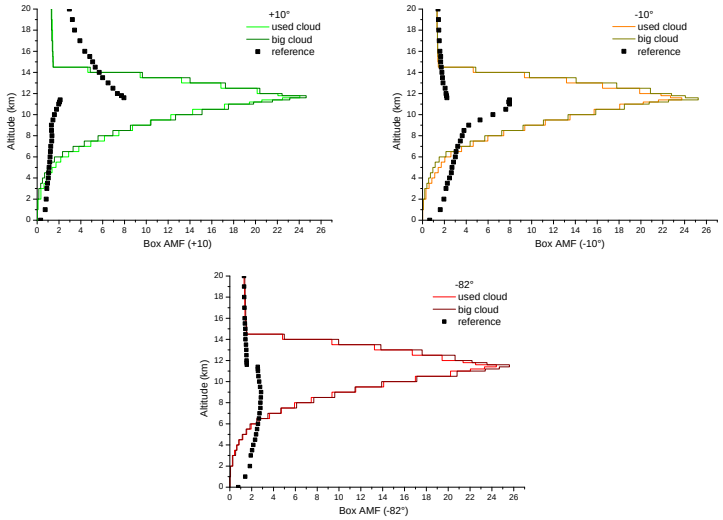

Fig. A1. Box AMF for the cloud top height of 14.5 km and a cloud extinction coefficient of 13 km^{-1}, for both the small cloud we used and a the bigger (more realistic) cloud. The difference between the two Box-AMFs is small. In addition the Box AMFs for the reference case are shown.

ACPD
13, 24343–24403, 2013

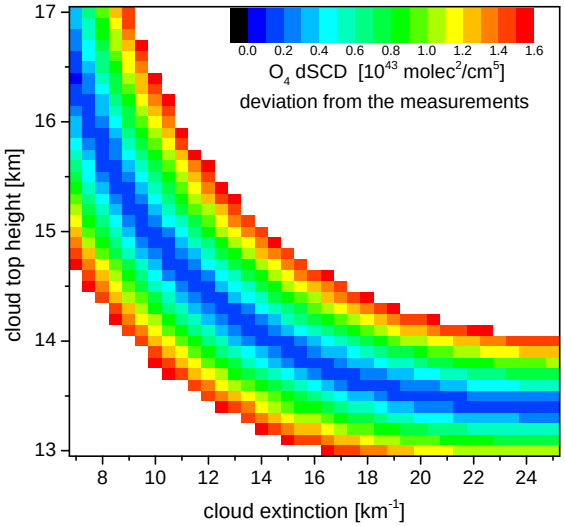

Fig. A2. Colour coded difference between the measured and the modelled O_4 SCD for the simulated range of cloud top heights and cloud extinctions. The minima describe a curve from 13.4 km to 16.7 km and from 25 km^{-1} to 7 km^{-1}

ACPD
13, 24343–24403, 2013

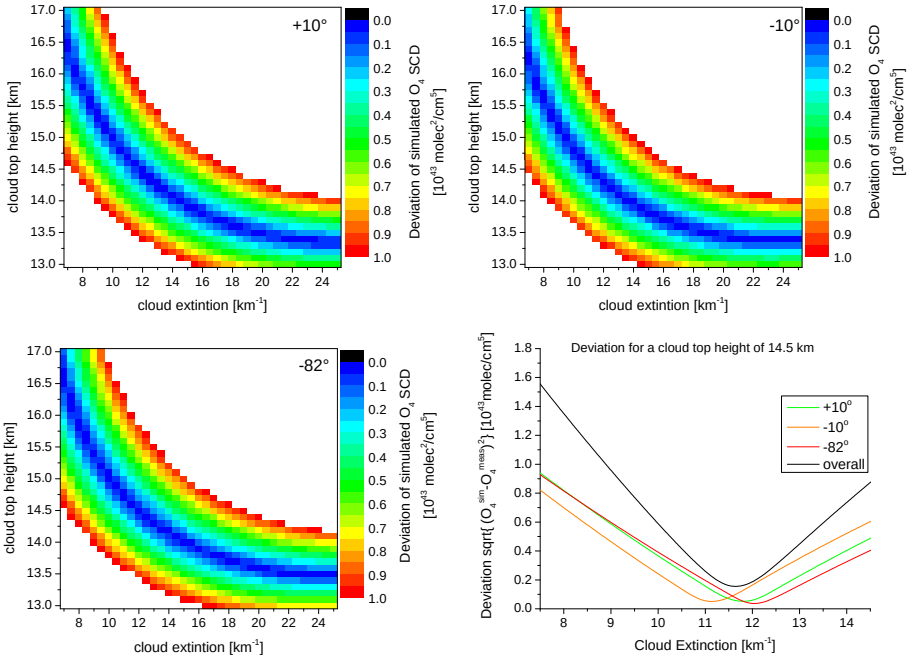

Fig. A3. Similar to Fig. A2, but for the individual viewing directions. A cross section for the cloud top height of 14.5 km is shown in the bottom left. The minima for the three viewing directions are not observed at exactly the same cloud extinction, which might be caused by a small error in the simulated reference SCD.

ACPD
13, 24343–24403, 2013

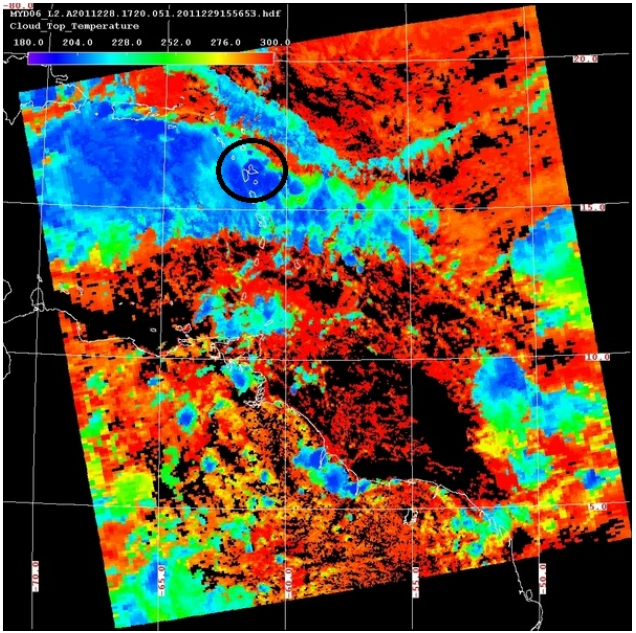

Fig. A4. Cloud top temperature observed by the MODIS instrument. In the area of interest (black circle 61.64° W 16.19° N) the cloud top temperature drops to ≈200 K

ACPD
13, 24343–24403, 2013